OBSERVATIONS OF
MID-OCEAN INTERNAL TIDES
DURING IWEX

by

MARLENE ANN NOBLE

B.S., University of Washington
(1969)

M.S., Princeton University
(1972)

SUBMITTED IN PARTIAL FULFILLMENT
OF THE REQUIREMENTS FOR THE
DEGREE OF MASTER OF SCIENCE

at the

MASSACHUSETTS INSTITUTE OF TECHNOLOGY

June, 1975

Signature of Author.....
Department of Meteorology
June, 1975

Certified by.....
Thesis Supervisor

Accepted by.....
Chairman, Departmental Committee

OBSERVATIONS OF MID-OCEAN INTERNAL TIDES DURING IXEX

by

Marlene Ann Noble

Submitted to the Department of Meteorology on June 17, 1975 in partial fulfillment of the requirements for the Degree of Master of Science

ABSTRACT

The internal tidal band measured by the IWEX tri-moor, a very stable platform against vertical motions located in the northwestern Atlantic (27°40'N, 69°53'W), is investigated in this thesis. The large phase changes with depth observed at the array site implied energy in the band was propagating toward the ocean floor. Conventional and maximum likelihood realizations of the wavenumber power spectra confirmed this result. Energy was propagating downward with vertical scales greater than 1.7 kilometers. The vertically integrated energy in that portion of the tidal field coherent with the surface tide was approximately 10 ergs/cm^2.

To facilitate comparison of our data with that of other investigators, the field was decomposed into normal modes, even though evidence indicated that the modal model does not strictly apply. Mode one's energy was dominant. The remaining energy was either in mode two or three, depending on the type of signal processed. Temporal variation of the field was reflected by the differing decompositions of the first and second half of the record. The scales found by this method were consistent with those found by maximum likelihood.

Thesis Supervisor: Terrence Joyce
Title: WHOI Scientist

ACKNOWLEDGMENTS

The authoress wishes to express her sincere appreciation for the guidance and insight provided by her thesis supervisor, Dr. Terrence Joyce. His interest in the project, coupled with the generous gift of his time, made working for him a distinct pleasure as well as a valuable experience.

She also wishes to thank the many people who gave of themselves so freely. Dr. Melbourne Briscoe was ever available for consultation. Ms. Nancy Bauchmann, whose knowledge of and experience with the IWEX data set and processing routines, was invaluable. Mr. Jim Richman not only provided the normal mode generation program; the discussions with him covering many aspects of internal wave theory are greatly appreciated. The efficient typists, May Reese, Audrey Williams and Doris Haight, also deserve our thanks. So does the Woods Hole Buoy Group, for the use of and assistance with their data processing programs.

Partial support of this work was sponsored by a contract with the Applied Physics Laboratory, The Johns Hopkins University, Contract #APL 37211.

TABLE OF CONTENTS

FIGURES

TABLES

1.0 INTRODUCTION

From the beginning of the observations of internal waves, oscillations at tidal frequency have appeared. A review of this early work is given by Defant (1949). But, at best, the initial observations present a limited picture of the total field. Records are both short, many of them cover a time period from several hours to several days, and spatially limited. Due to measurement difficulties, most observations are concentrated near coastal regions and in the upper part of the water column. To minimize contributions from the surface tide, measurements deal most often with the temperature field. With six days of record, Reid (1956) found internal tides off the California coast. Maeda (1971) observed the upper 200 meters of the temperature field in the eastern Pacific (29°N, 135°E). He found internal tides propagating off the shelf.

With the advancement in mooring technology, it became possible to obtain a long series of measurements from both coastal and mid-oceanic stations. For the first time, a statistical treatment of the data could be undertaken to determine the persistence, bandwidth, modal distribution and propagation characteristics of the field. At 'Site D' (39°N 70°W), Magaard and McKee (1973) analyzed two months of current meter record to determine the modal structure of the M_2 internal tide. A comprehensive account of the present state of knowledge concerning internal tides is given by Wunsch (1975).

Recently Ross Hendry (1975) has analyzed several months of record from the MODE experiment in the northwestern Atlantic. The M_2 component of the internal tides was found to dominate adjacent S_2 and N_2 frequency bands. Working mainly with temperature sensors, the portion of the M_2 internal tide coherent with the equilibrium tide was decomposed into normal modes. The energy was concentrated in mode 1. A horizontal wavenumber estimate of mode 1's energy implied the waves were propagating toward the southeast.

In the following, data from the IWEX trimoor (Briscoe (1975)) located in the same general region of the northwestern Atlantic, is analyzed for semidiurnal internal tides. Mooring motion is shown to be an insignificant contaminant of the temperature signal. Through WKBJ and maximum likelihood techniques, a consistent picture emerges showing energy propagating toward the ocean floor. To facilitate comparison of our results with other data, modal analyzing of the field is also presented.

2.0 DATA SET

The data used in this investigation was part of a set obtained during the internal wave experiment (IWEX). A heavily instrumented subsurface trimooring was anchored in the northwest Atlantic (27°40'N 69°53'W), as shown in figure 2.1. The experiment lasted 40 days, from November 3 to December 11, 1973. On each of the three legs (A,B,C), instruments were attached in a logarithmic pattern as depicted in figure 2.2. Between 578 meters and 1018 meters, vector averaging current meters (VACM's) were used to measure horizontal currents and absolute temperatures. These were modified to record differential temperature over a vertical separation of 1.74 meters. Unmodified 850-T meters were used in the deeper waters. Additional temperature information was supplied through temperature-pressure (TP) recorders of the type described by Wunsch and Dahlen (1973). Table 2.1 lists the instruments and their positions on the mooring. A1 refers to instrument 1 on leg A, etc.

The trimoor provided a remarkably stable platform against vertical motion. A more detailed analysis of vertical excursions at tidal frequency (.08 cpd) will be presented in a later section, but, initially, our time series of pressure from TP recorders is presented in figure 2.3. The first record is from the top of the mooring. Note the extremely small vertical excursions. The small oscillations in the record are, in fact, largely pressure effects from surface tides, for they are of approximately the right frequency and amplitude (30 cm). Even at mid-depths (A12)

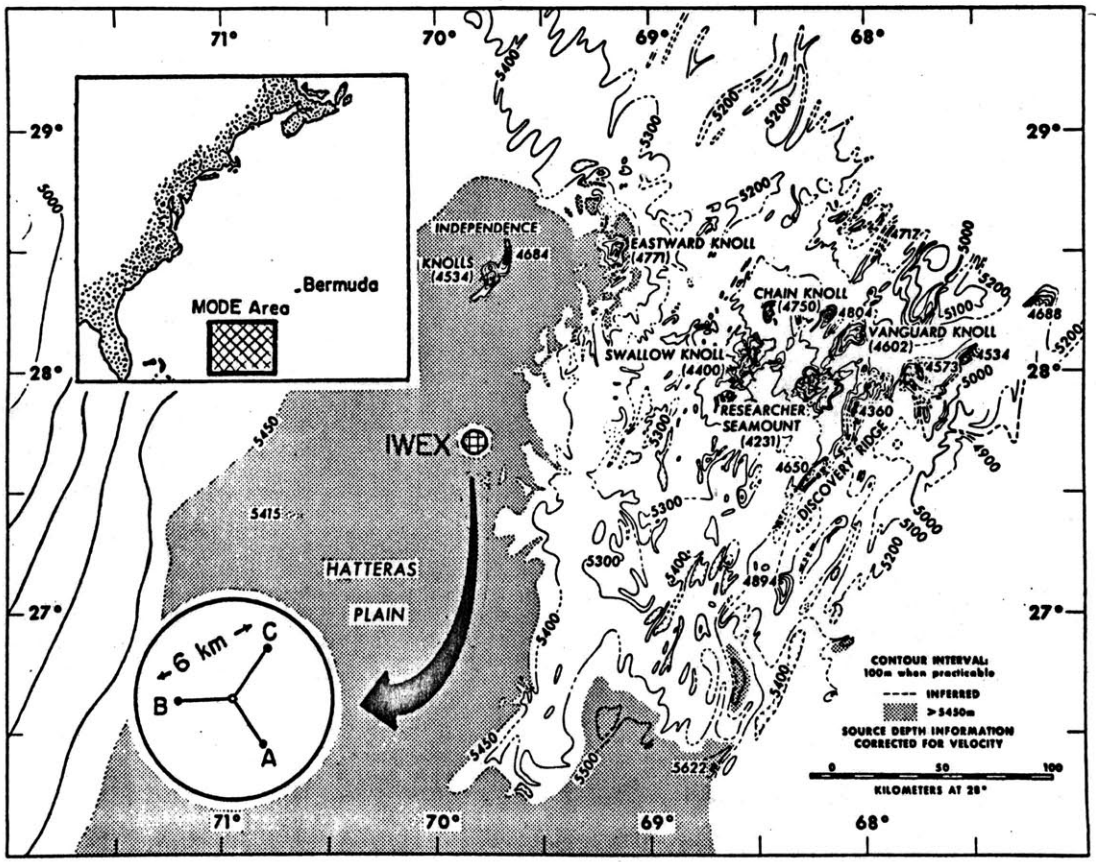

2.1 Bathymetry of the northwestern Atlantic Ocean. IWEX site and MODE area are indicated.

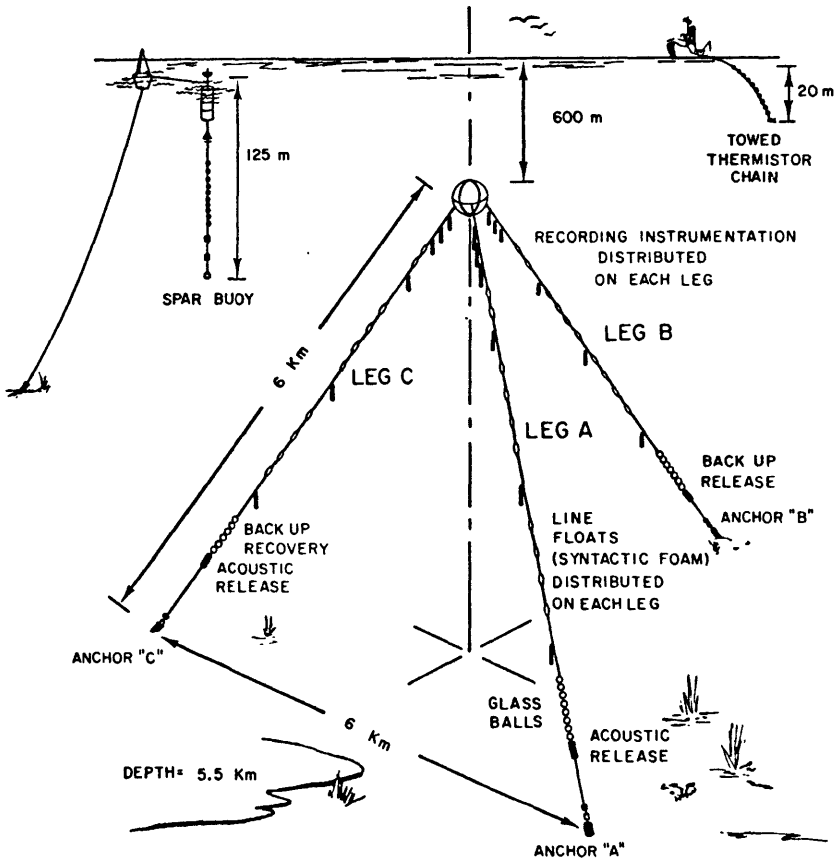

TRIMOORED INTERNAL WAVE
EXPERIMENT (IWEX)

2.2 Structure of IWEX tri-moor

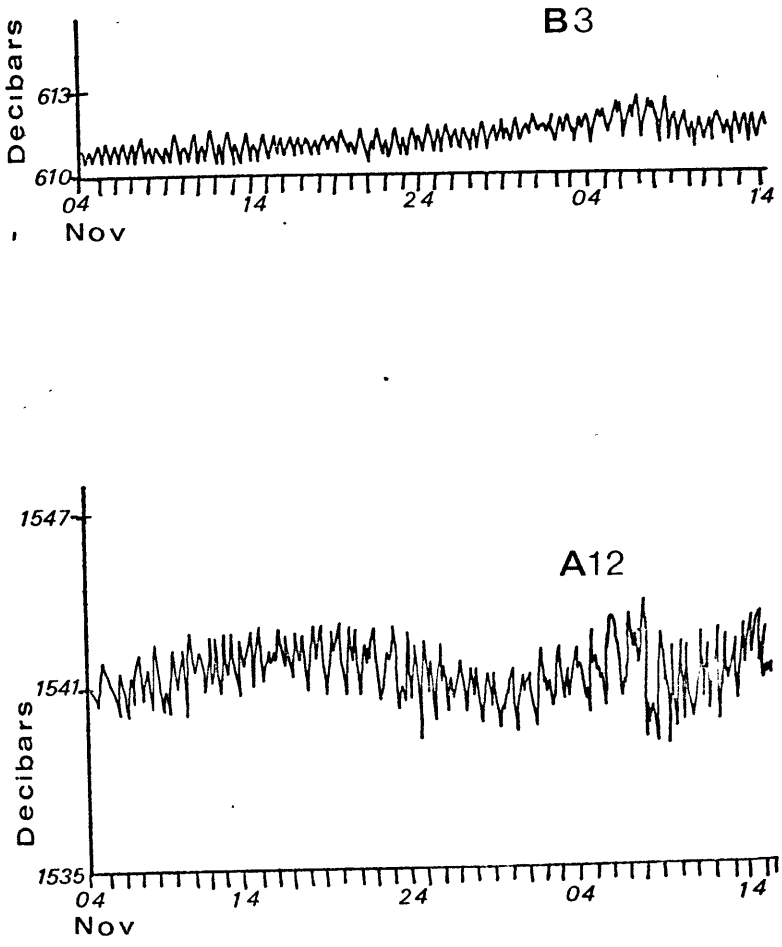

2.3a Pressure time series for B3 and A12

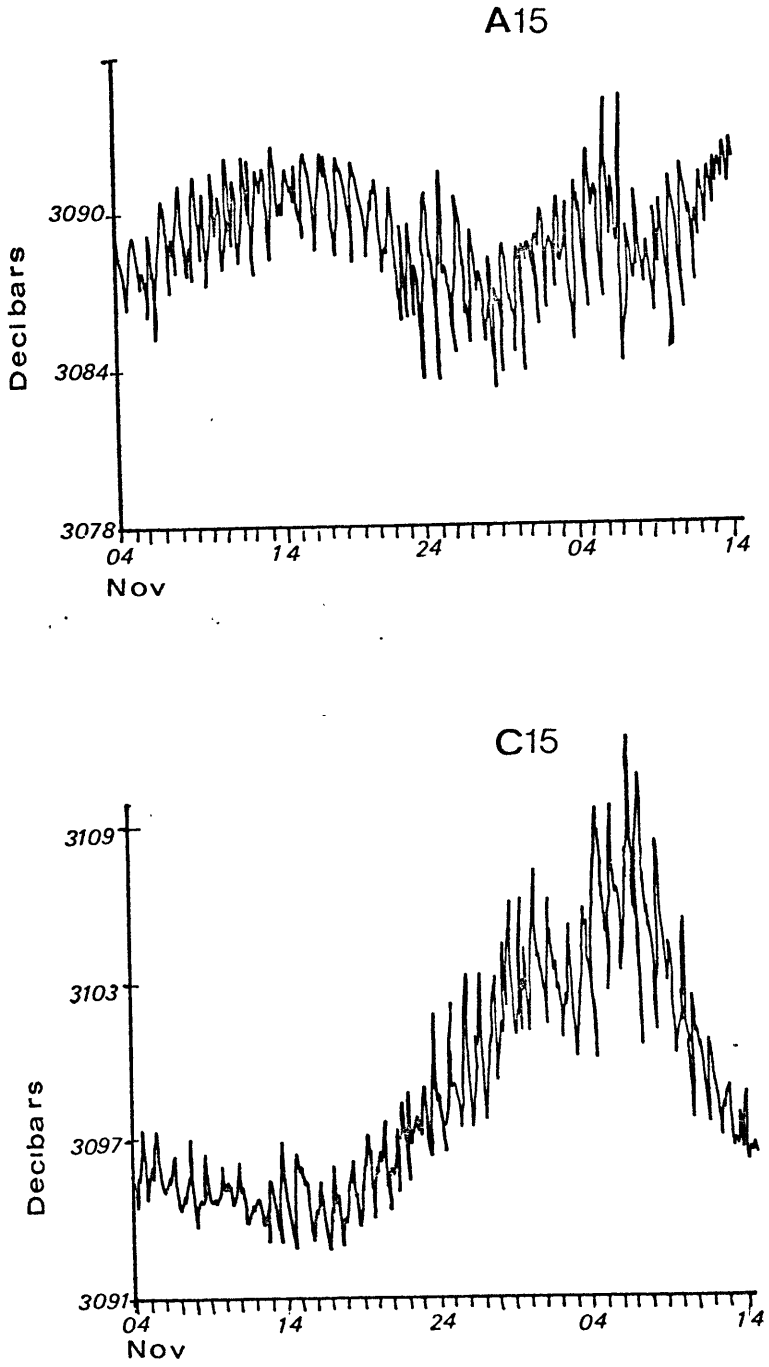

2.3b Pressure time series for A15 and B15

Table 2.1

TRI-MOOR - INSTRUMENT PLACEMENT

(M) Depth	(M) Line Position	Instruments Leg A		Instruments Leg B		Instruments Leg C	
598	5.5	A-1	M-VACM	B-1	Pinger	C-1	M-VACM
600	8.1	A-2	M-VACM	A-2	M-VACM	C-2	M-VACM
600	11.3	-	-	B-3	Pressure Rec.	C-3	Pressure Rec.
605	15.9	A-4	M-VACM	B-4	M-VACM	-	-
633	47.9	A-5	M-VACM	B-5	M-VACM	C-5	M-VACM
724	153.9	A-6	M-VACM	B-6	M-VACM	C-6	M-VACM
1003	483.2	A-7	Inclinometer	B-7	Inclinometer	C-7	Inclinometer
1008	487.0	A-8	M-VACM	-	-	-	-
1009	490.2	A-9	Pressure Rec.	B-9	Pressure Rec.	C-9	Pressure Rec.
1017	497.2	A-10	M-VACM	B-10	M-VACM	C-10	M-VACM
1018	500.4	A-11	Tension Rec.	-	-	-	-
1527	1103.1	A-12	Pressure Rec.	-	-	-	-
2044	1720.2	A-14	850 T	B-14	850 T	C-14	850 T
3041	2943.7	A-15	Pressure Rec.	B-15	Pressure Rec.	C-15	Pressure Rec.
4021	4175.0	A-16	850 T	-	-	-	-
5124	5663.0	A-17	Tension Rec.	B-17	Tension Rec.	C-17	Tension Rec.

the excursions are less than five meters, with an average of two meters. As might be expected from such a mooring, the deeper pressure records indicate greater vertical motion. Oscillations in the tidal band average 6-12 meters, with a low frequency amplitude of about twice this.

In order to determine the proper frequency bandwidth for tidal analysis, auto and cross spectra of currents and of temperatures were computed for several record lengths. Each was chosen to minimize leakage from the local inertial peak (25h), as well as emphasize the tidal peak. As shown in table 2.2, the coherence characteristics of the field remain fairly independent of bandwidth. In the autospectra the tidal peak also dominates, independent of resolution. Coupling the statistical nature of the problem with a relatively short data set (40 days), we were forced to accept poor resolution in exchange for reasonable stability.

Even with this wide bandwidth, the characteristics of the field are expected to be largely determined by the M_2 tidal component. From data collected during a large scale experiment (MODE) in the vicinity of the IWEX mooring, Hendry (1975) found M_2 energies three times larger than N_2 or S_2, for depths less than 3400 m. The structure of the adjacent frequency bands was very similar to that of M_2, suggesting that much of the S_2 and N_2 energies are due to shifted M_2 energies.

Doppler shifting also broadens the tidal bandwidth. The true frequency (σ_0) can be shifted by low frequency currents

TABLE 2.2

Coherence Stability as a Function of Resolution

Instruments	Piece length hours	Coherence	Phase	Variance**	0 coh level**
A4 E*N*	75	.66	110	±.23	.51
	150	.52	141	±.36	.72
	234.4	.68	129	±.34	.86
A4E-B4N	75	.66	102	±.23	.51
	234.4	.68	131	±.34	.86
A4E-B4E	75	.98	- 1.2	0	.51
	234.4	.99	0	0	.86
A4N-B4E	75	.66	-98	±.23	.51
	234.4	.63	-132	±.36	.86
A4N-B4N	75	.95	1.2	±.03	.51
	234.4	.98	-1.	0	.86
A10U*B10U	75	.97	-2.3	0	.51
	150	.99	-3.	0	.72
	234.4	.99	-3.	0	.86
A14U-B14U	75	.87	-14	±.08	.51
	150	.96	-14	±.06	.72
A5U-B10U	75	.55	3.8	±.27	.51
A5U-A10U	150	.59	13	±.36	.72
A6U-A10U	75	.74	15.2	±.20	.51
B6U-B10U	150	.79	8.	±:22	.72

*U = up displacement
E = east current component
N = north current component
**95% level confidence

according to the relation

$$\sigma_m = \sigma_0 + U_0 \, k$$

where k is the horizontal wavenumber of the process investigated. For a typical wavelength in the tidal band (140 km), a current of 9 cm/sec will shift M_2 to the S_2 frequency.

A look at the energy field is also presented. Estimates of time averaged horizontal kinetic and potential energies were obtained by averaging three 75 hour overlapped pieces. From the formula (Phillips 1968)

$$\overline{PE} = 1/4 \; N^2(z) \; \xi^2(z) \; \rho_0$$

$$\overline{KE} = 1/4 \; \rho_0 (u^2 + v^2)$$

These energies were vertically averaged. Care must be taken in the interpretation of the kinetic energy, for it is contaminated by the barotropic tide. Figure 2.4 shows a low frequency modulation of the tidal energies. The kinetic and potential tend to mirror each other. This variability in the partition of energy indicates the field may be changing composition during the course of the experiment. This will be discussed in a later seciton. Also note the general rise in total energy with time.

Due to the above considerations the 75h piece length was decided upon, as this gave the most statistical reliability without unacceptable loss of resolution. The shorter pieces had the additional advantage in that the temporal evolution of the tidal field could be monitored.

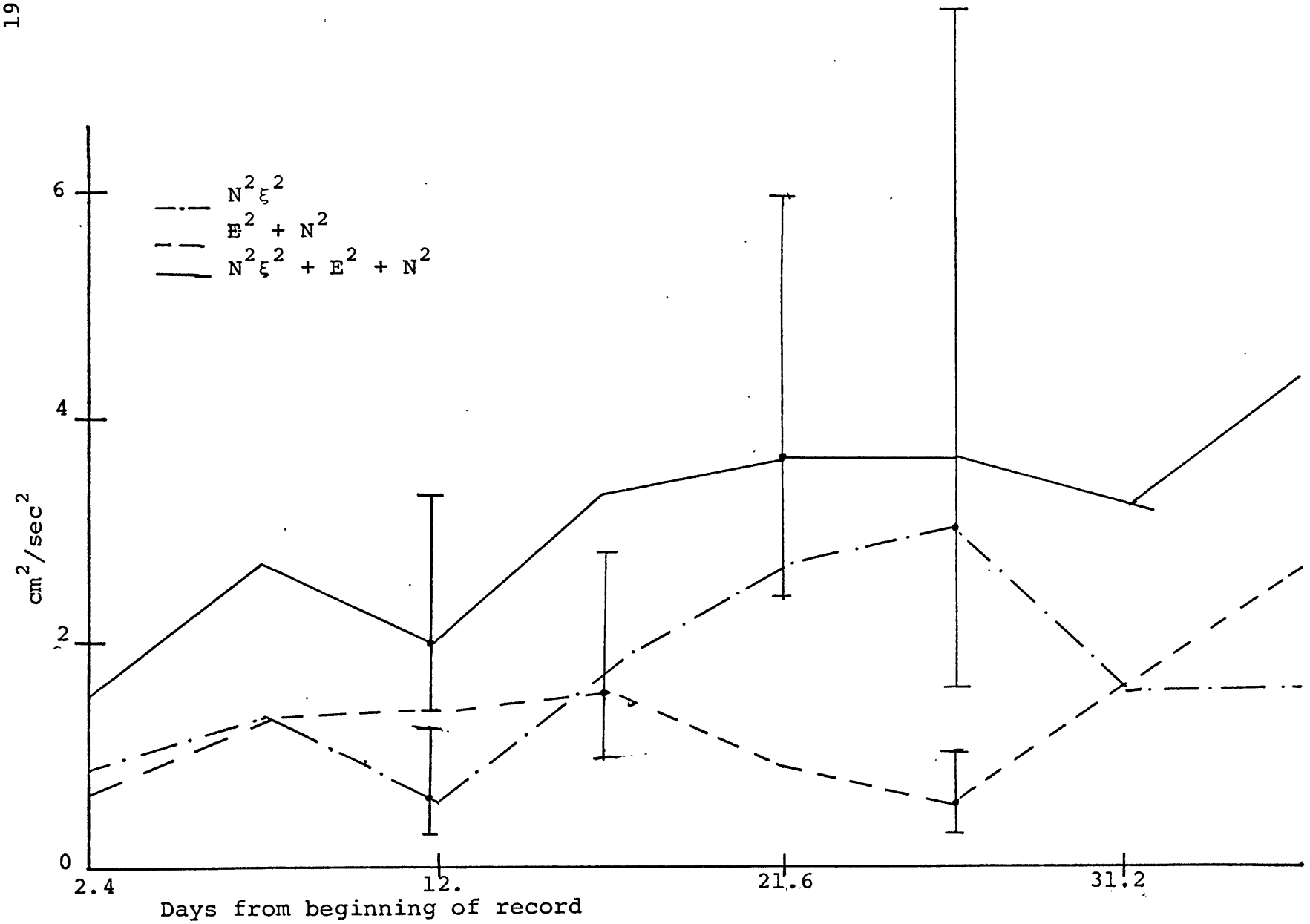

2.4 Energy time series. The confidence limits for relevant points are indicated.

For the actual processing, an ensemble average was formed from segments 75 hours long, each containing 1200 data points. A Hanning data window (cosine arch) was applied to each segment. The resultant spectral estimate was renormalized by 8/3. To retain as much of the original information as possible, the segments were overlapped 50%, giving a total of 25 pieces, but only 13 distinct ones. The temperature spectra were converted to isotherm displacement (Up) spectra by dividing them by the square of the 40 day mean temperature gradient.

The tidal coherence scales for the mooring are presented in table 2.3. Statistical confidence limits for the various cross spectra are subject to some ambiguity, for in this calculation a white noise process is assumed, where each segment, or frequency band, is independent of its partners. There are fewer problems for the autospectra confidence intervals. Nuttall (1971) has shown that the 50% overlapped, Hanned processing returns nearly all the original information. From 13 independent pieces, there are 26 degrees of freedom available.

Due to the large horizontal scales and small horizontal bandwidth of the internal tides (Munk and Phillips (1968)), only minor drops in coherence are observed even for the largest horizontal separations. Vertical coherence, or more specifically slant coherence, is greatly affected by increasing vertical separations. For the currents, the significance level for zero coherence occurs at 120 meters. This scale is more than tripled for the Ups, where the coherent field extends vertically to 400 m.

TABLE 2.3

Coherence scales for the IWEX tri-moor

Instruments	Horizontal Separation (m)	Vertical Separation (m)	Coherence*	Phase
A4E-B4E	14	0	.98	- 1.2
A14E-B14E	1599	0	.847	- 3.1
A2E-A4E	3.2	4.9	.80	- 4.4
A10E-B10E	450	0	.769	2.2
A2E-A6E	75.4	124.9	.63	-15.2
A4E-A6E	72.2	120.0	.544	-16.5
B6E-B10E	179.7	292.5	.391	20.3
A4E-A10E	251.9	412.5	.30	-67.8
A2E-A10E	255.1	417.4	.19	-11.4
A4U-B4U	14	0	1.0	- .3
A2U-A4U	3.2	4.9	.99	1.0
A6U-C6U	139.1	0	.99	- 1.0
A10U-B10U	560.3	0	.975	- 2.3
A14U-B14U	1599	0	.873	-14.0
A2U-A6U	75.4	124.9	.84	.2
B4U-B6U	72.2	120.0	.835	- 3.5
B6U-A10U	179.7	292.5	.742	15.2
A4U-A14U	915.4	1439.8	.550	68.6
A5U-B10U	273.6	383.6	.549	3.8
C6U-B14U	966.2	1319.8	.55	64.7
C10U-B14U	1077.3	1027.3	.582	50.5
B4U-B10U	251	412.5	.485	- .7
A2U-A10U	255	417.11	.457	14.9

*For all instrument pairs, the 95% confidence level for zero coherence is .51 .

3.0 MOORING MOTION AND COHERENT SIGNAL EXTRACTION

The pressure recorders introduced in the previous section indicate the mooring is stable against vertical motions. Here, a model is developed to estimate the amplitude of vertical instrument motion as a function of depth. The pressure, barotropic tidal, and temperature signals are modeled analytically. The parameters of each signal are solved for in terms of each signal's energy and the cross spectra among them. The values for the latter are computed from oceanic data. With this procedure, the contamination of the temperature signal due to instrument motion can be calculated. The noise is removed from the portion of the temperature signal coherent with the surface tide. This relatively noise-free signal is used in later sections to provide information concerning energy propagation and the modal decomposition of the internal tidal field.

Pressure Decomposition

In order to develop the proper analytic form for the pressure signal, the tidal frequency pressure field is decomposed into atmospheric (P_A), surface tidal (P_ξ), internal wave ($P_{I\omega}$) and mooring motion (P_{mm}) components. The relative magnitudes of each are estimated. Only those components judged significant are included in the analytical model of the pressure signal. The magnitude of the Fourier transform of the surface tide, $pg\xi$, is used to scale all pressures; therefore $P_\xi = 1$.

Atmospheric tides are mainly S_2. Cartwright (1966) and Zetler (1971) have estimated the ratio of atmospheric to

oceanic S_2 to be 17%. Zetler, et al. (1975), have calculated the tidal coefficients for this area.

The S_2/M_2 ratio is 20%. This gives the relative amplitude of P_A as 3.4%, which can be neglected.

An upper bound on the pressure due to internal waves is also calculated. Both surface and internal waves satisfy

$$- i\sigma u - fv = -1/\rho \, P_x$$

$$- i\sigma v + fu = -1/\rho \, P_y$$

Since their respective currents are approximately equal, $k_\xi P_\xi / k_{I\omega} P_{I\omega}$ will be of order one. A length scale for internal tides is based on a numerical computation of MODE one, which is calculated from the density profile of the IWEX area. The wavenumber $(k_{I\omega})$ is $.375 \times 10^{-4} m^{-1}$. From the dispersion relation, the surface wave number is

$$k_\xi = \sigma/\sqrt{gh} \simeq .6 \times 10^{-6} m^{-1} .$$

This implies the pressure from each relevant mode is approximately 2% of the surface tide. Since higher modes have larger wave numbers, and, for random phased modes, their pressure signals would interfere, $P_{I\omega}$ is also neglected in the decomposition.

Initially, pressure due to instrument motion can only be roughly estimated, since it is the result of an unknown coupling between tidal currents and the mooring. But to develop a pressure signal of amplitude comparable to the surface tide, an

instrument has only to be displaced vertically 30 cm; this contribution can be large.

From the above, it can be seen that the only significant contributions to the measured pressure signal are due to the surface tide and to mooring motion. Only these elements will be included in the decomposition.

Analytic Model

The analytic expression for the cross spectra among pressure, surface tidal and temperature signals are derived below. The Fourier transform of each signal is modeled as

$$\text{Tide} = \xi \qquad \text{(displacement units)}$$

$$\text{Pressure} = (1 + \alpha)\ \xi + M \qquad \text{(displacement units)}$$

$$\text{Temperature} = -\Gamma\{(\beta + \alpha + r)\ \xi + T + M\} \qquad (^{\circ}C)$$

where

ξ = Fourier transform of the generated surface tidal signal

$\alpha\xi$ = mooring motion coherent with the surface tide
$= (a + ib)\xi$

M = mooring motion incoherent with the surface tide

$\beta\xi$ = isotherm deflection due to internal waves coherent with the surface tide
$= (c + id)\xi$

T = isotherm deflection due to internal waves incoherent with the surface tide and with M

$r\xi$ = isotherm deflection due to surface tide

Γ = temperature gradient

$i = \sqrt{-1}$

The set of cross spectral relations are

$$|coh_{Tide\ Pres}| = 1/(1+m^2/(1+\alpha)^2)^{\frac{1}{2}} \tag{3.1a}$$

$$cospectrum_{Tide\ Pres}/\xi^2 = (1+a) \tag{3.1b}$$

$$Quad_{Tide\ Pres}/\xi^2 = -b \tag{3.1c}$$

$$(Pressure)^2/\xi^2 = (1+\alpha)^2 + m^2 \tag{3.1d}$$

$$|coh_{Tide\ Temp}| = 1/\left(1 + \frac{t^2}{(\beta^2+\alpha^2r^2)} + \frac{m^2}{(\beta^2+\alpha^2+r^2)}\right)^{\frac{1}{2}} \tag{3.2a}$$

$$cospectrum_{Tide\ Temp}/\xi^2 = -\Gamma(r+a+c) \tag{3.2b}$$

$$Quad_{Tide\ Temp}/\xi^2 = \Gamma(b+d) \tag{3.2c}$$

$$(Temperature)^2/\xi^2 = \Gamma^2\{(\beta+\alpha+r)^2 + m^2 + t^2\} \tag{3.2d}$$

$$coh_{Pres\ Temp} = \left\{\frac{-(1+\alpha)^*\ \ (\beta+\alpha+r)}{|(1+\alpha)|\ \ |(\beta+\alpha+r)|} - \frac{m^2}{|(1+\alpha)|\ \ |(\beta+\alpha+r)|}\right. \tag{3.3a}$$

$$\left. \times\ |coh_{Tide\ Temp}| x |coh_{Tide\ Pres}|\right.$$

In the above relations, M and T have been scaled by the tidal amplitude (ξ), to give m and t. In each set, b and c imply a.

With sets 3.1 and 3.2, there are six independent relations. We solve for six unknowns, α, β, $|m|$, $|t|$, in terms of spectral energies and coherences. A consistency check is supplied by equation 3.3a, for the pressure-temperature coherence can both be derived from the above parameters and measured directly.

TABLE 3.1

Input Parameters for Generated Tidal Signal

Tidal Component	Amplitude cm	Phase* deg.
Q_1	1.3	191.0
O_1	6.22	196.0
P_1	2.40	194.9
K_1	7.79	194.5
N_2	8.20	339.1
M_2	34.57	0.7
S_2	6.77	32.7
K_2	1.82	32.0

*Phase is Greenwich epoch.

The temperature and pressure fields are measured by the TP recorders. The barotropic tidal signal (ξ) is generated by a numerical routine from the previously mentioned tidal constants.

$$\xi(n\Delta t) = \sum_i A_i \sin (2\pi f_i (n\Delta t) + \theta_i)$$

where

A_i = amplitude of the i^{th} component

f_i = frequency of the i^{th} component

θ_i = phase of the i^{th} component

Δt = time step

Table 3.1 lists the relevant input parameters for the above signal.

The energies and cross spectral values of the above signals are substituted into the set of equations 3.1 and 3.2. The unknown parameters are solved for. The resultant amplitudes are listed in Table 3.2. Note, for all instruments, the isotherm deflection due to mooring motion (α and m) is significantly less than that due to internal waves. Excepting C15, the consistency check indicates the model applies everywhere. The fact that the measured coherence for the deeper instrument is larger than the calculated suggests there exists a significant correlation between the incoherent temperature signal (t) and the incoherent mooring motion (m) . Inspection of the pressure

TABLE 3.2

Pressure and Temperature Signals Deduced from the Mooring Motion Model. The Coherence Consistency Check is also depicted

	Pressure*$_{mm}$		Temperature*		Coherence$_{PT}$	
Ins	α	|m|	β	|t|	Calculated	Measured
C3	$.44e^{i99°}$	.2	$7e^{-i95°}$	10.7	$.56e^{i118°}$	$.53e^{i118°}$
A9	$.34e^{+17°}$	.73	$9.24e^{-i62°}$	10.2	$.66e^{i123°}$	$.50e^{i120°}$
C9	$.30e^{-i90°}$	.57	$7.65e^{-i65°}$	8.5	$.62e^{i140°}$	$.54e^{i141°}$
A12	$1.0e^{+i36°}$	1.03	$12.4e^{-i30°}$	17.5	$.56e^{i138°}$	$.59e^{i123°}$
A15	$2.8e^{+i58°}$	1.8	$14.8e^{+i27°}$	23.	$.49e^{i162°}$	$.57e^{i155°}$
C15	$1.2e^{-i90°}$	2.62	$14.9e^{+i24°}$	24.	$.31e^{i125°}$	$.69e^{i108°}$

*All amplitudes scaled by ξ = 29 cm. Phases are measured with respect to the generated tidal signal.

records in figure 2.3 indicates that C15 which has the largest discrepancy in the consistency check, also undergoes the largest mooring motion.

Coherent Up Signal

Since the consistency check indicates this model applies over the full IWEX mooring, the temperature signal for all IWEX instruments can be modeled as $T = - \Gamma (\beta+\alpha+r) \xi + t'$, where t' represents all incoherent isotherm motion. The coherent mooring motion (α) is extrapolated from parameters for each mooring leg. Using relations 3.2, a relatively noise-free Up signal can be determined. The isotherm (amplitudes, phases) with their respective energies, are listed in Table 3.3. Note the phase shift with depth. The deeper instrument consistently leads, indicating upward phase propagation. This will be investigated in the next section. The potential energies are depicted in figure 3.1. The numerical values are calculated from

$$P E = \rho_0 N^2(z) \xi^2(z)/4 .$$

The incoherent potential energy may also be directly calculated from the data, for

$$\gamma_{\text{Tide Temp}} = \frac{- \Gamma(\beta+\alpha+r) \xi\xi^*}{\Gamma(\xi\xi^*)^{\frac{1}{2}}(|\beta+\alpha+r|^2\xi\xi^* + t't'^2)^{\frac{1}{2}}} \qquad (3.4)$$

if we call $(\Gamma t')^2$ the incoherent energy and $\Gamma^2|\beta+\alpha+r|^2 \xi\xi^*$ the coherent energy, then

TABLE 3.3

The Amplitude, Phase and Energy of the Temperature Signal Derived from Mooring Motion Model

Ins	Isotherm displacement* Coherent**(β)	Incoherent(t)	Energy density (ergs/cm^3) Coherent	Incoherent	Total
C3	$6.96e^{-i64°}$	10.6	.196	.456	.652
A4	$7.4e^{-i64°}$	11.7	.222	.556	.777
A6	$10.5e^{-i49°}$	10.2	.512	.483	.995
A9	$9.2e^{-i34°}$	8.65	.231	.204	.435
C9	$7.74e^{-i33°}$	8.5	.164	.197	.361
A10	$9.36e^{-i30°}$	8.9	.238	.216	.454
A12	$12.6e^{+i1°}$	17.5	.065	.126	.191
A14	$12.6e^{+i26°}$	25.0	.048	.189	.237
C14	$17.2e^{+i19°}$	23.4	.089	.166	.255
A15	$12.7e^{+i51°}$	23.0	.028	.092	.120
C15	$15.4e^{+i53°}$	24.6	.039	.105	.144

*Amplitude scaled by ξ = 29 cm.

**Positive phase indicates the signal leads the tide.

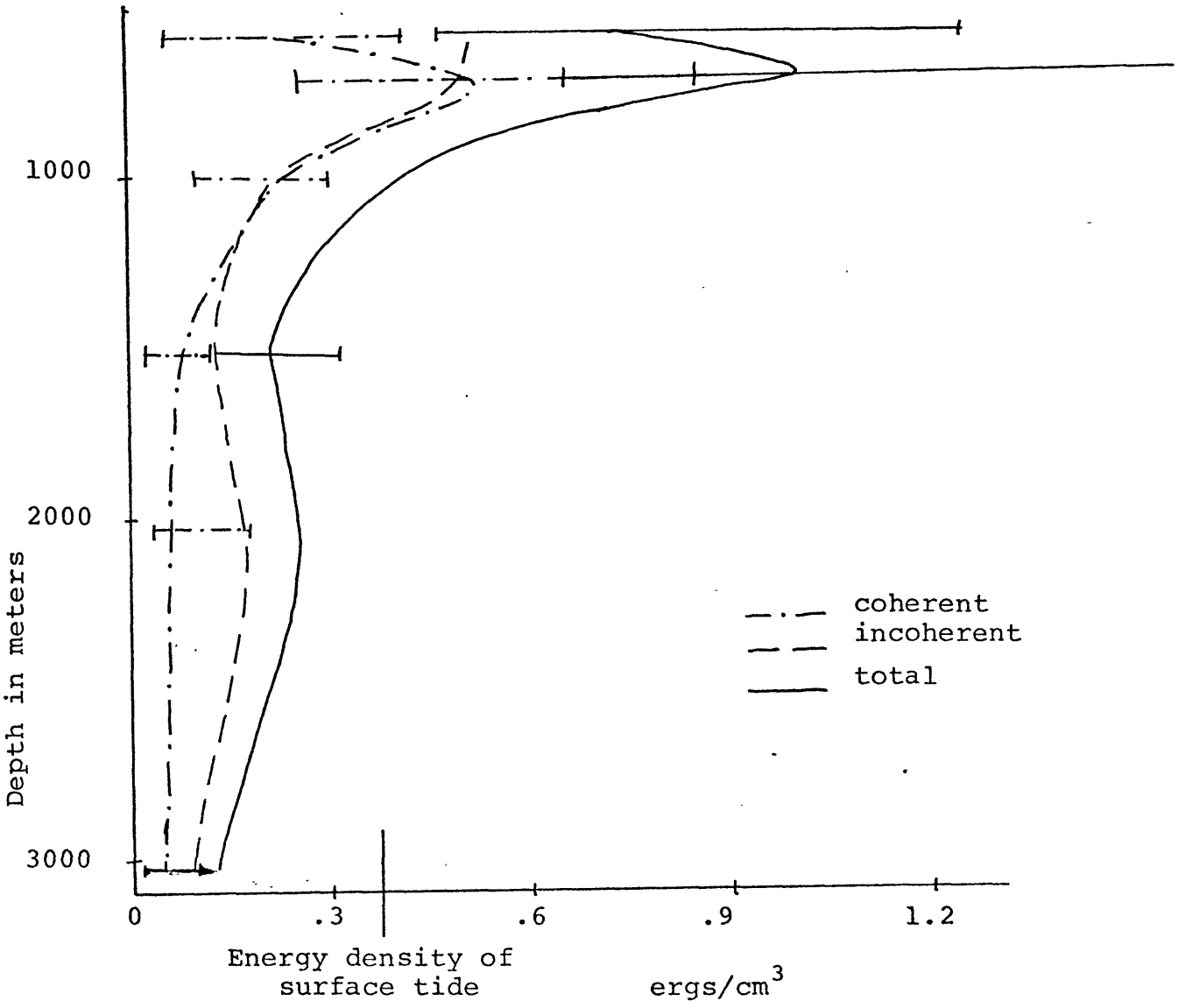

3.1 Potential energy profiles for isotherm displacements which are coherent and which are incoherent with the surface tide

$$PE_{inc} = (1-\gamma^2)PE_{total} = (1-\gamma^2)(\tfrac{1}{4}\rho_0 N^2(z)\xi^2_{tot}(z)) \qquad (3.5)$$

where γ is the coherence between tide and ups. This gives approximately the same numerical values for energy and a basis from which to calculate confidence limits. The surface tidal energy density, noted on the graph, is calculated from

$$\overline{En}_{surface} = \tfrac{1}{4}\frac{\rho_0 g \xi^2}{H}$$

where ξ is the surface deflection based on the generated tidal signal.

By extrapolating the energy profiles of figure 3.1, the depth integrated energy density can be estimated.

$$\overline{PE}_{coh} \cong 3.8 \times 10^4 \text{ ergs/cm}^2$$

$$\overline{PE}_{tot} \cong 1. \times 10^5 \text{ ergs/cm}^2$$

where $\overline{PE}_{coh}$ is the vertically integrated potential energy in the coherent field. $\overline{PE}_{tot}$ represents the total field.

The partition of energy for a simple propagating wave is

$$\frac{\overline{KE}}{\overline{PE}} = \frac{\sigma^2 + f^2}{\sigma^2 - f^2} \qquad (3.6)$$

Using relation 3.6, the total energy in the internal tidal field can be solved for

$$\overline{En}_{coh} \cong 1. \times 10^5 \text{ ergs/cm}^2$$

$$\overline{En}_{tot} \cong 2.6 \times 10^5 \text{ ergs/cm}^2$$

These energy values can be used to estimate the energy scale for the wavenumber spectrum derived in section five.

4.0 VERTICAL STRUCTURE AND PHASE PROPAGATION

The Brunt Väisälä profile shown in figure 4.1 has a maximum at seven hundred meters. A similar maximum is found in the potential energy field coherent with the surface tide, which was discussed in the previous section (figure 3.1). This suggests that a WKBJ approach may be a valid approximation to the field.

To test this assumption, the potential energy is divided by the local Väisälä frequency. The resultant is graphed in figure 4.2. If the WKBJ approximation is valid, then $N\xi^2$ should be uniform with depth (see appendix). Within the error bars, a straight line can be drawn through both coherent and incoherent fields. Only approximate agreement with the prediction is expected, for vertical scales larger than allowed by WKBJ occur in the internal tides, as will be shown in succeeding sections. Note figure 3.1 and figure 4.2 indicate the coherent and the incoherent, or noise, fields have similar structures. This might be expected, since doppler and nonlinear interactions may affect the internal tides enough to alter their coherence properties, but are not strong enough to radically alter their vertical structure.

The vertical distribution of horizontal kinetic energy with depth is presented in figure 4.3. The vertical resolution is poor, for there are fewer sites for current meters than for temperature recorders. The currents contain contributions from the surface tide as well. Both profiles show energy concentrated in the upper 1500 meters, with the maximum deeper for currents than for temperature. These energies are listed in table 4.1.

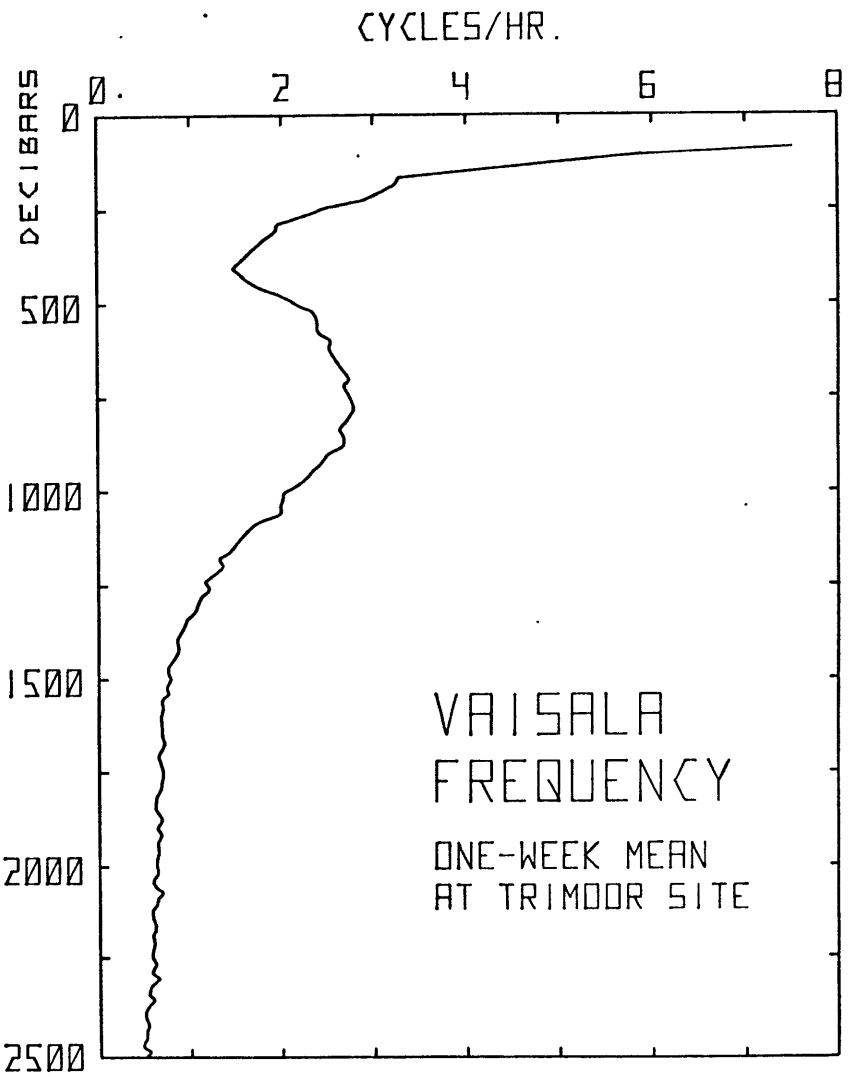

4.1 Brunt Väisälä profile for IWEX area

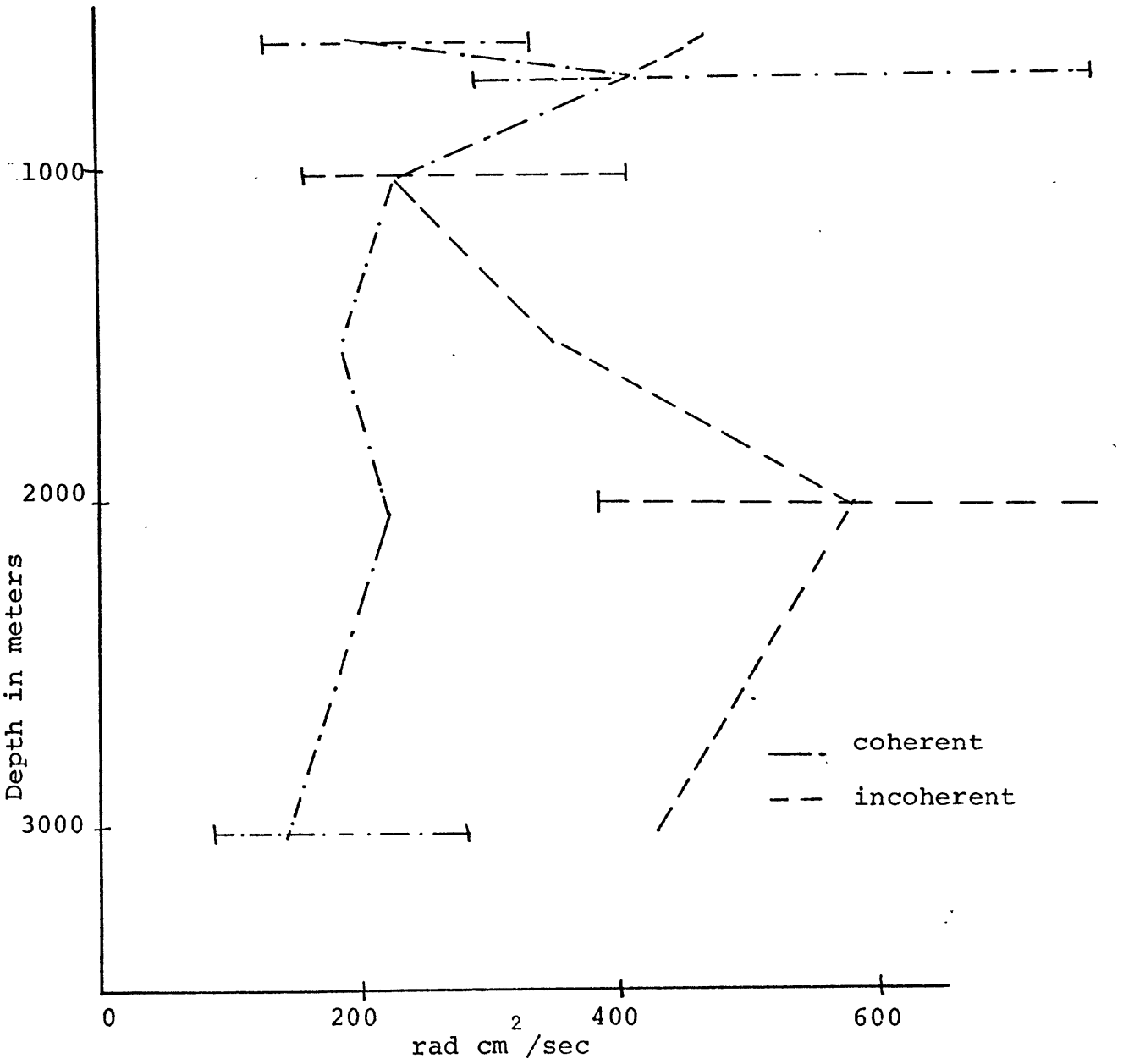

4.2 Isotherm displacements scaled in a WKBJ manner($N\xi^2$)

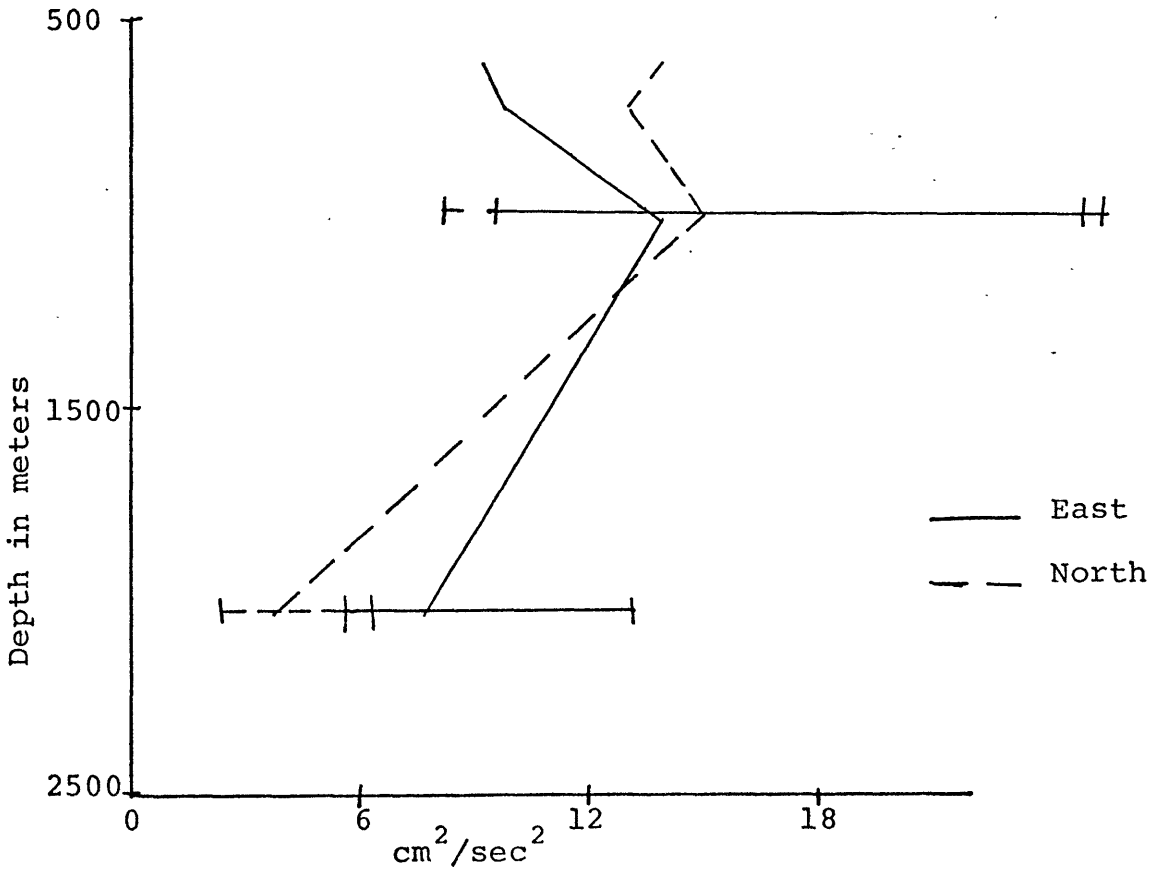

4.3 Squared horizontal current profile

Two methods of modeling internal tides appear in the literature. For mid-oceanic waves, a modal description of the field is popular. For each mode, as we traverse the water column, the phase changes by $\pm\pi$ through a modal node. With an infinite sum of randomly phased modes, any vertical phase distribution can be fit. The field can also be modeled as a sum of rays with differing horizontal wavenumbers. For a single ray, WKBJ implies the phase change between two instruments separated in the vertical is

$$\Delta\phi_{ab} = \pm \frac{k_H}{(\sigma^2 - f^2)^{\frac{1}{2}}} \int_a^b N(z)\, dz \qquad (4.1)$$

where

$\Delta\phi_{ab}$ = phase change

a,b = instrument positions

For a field dominated by a single ray, a plot of $\Delta\phi_{ab}$ vs $\int_a^b N(z)\,dz$ would be a straight line. This does not hold for a modal description of the field.

The phase change between instruments is measured directly by cohering Up records against each other. To prevent interference from the surface tide, only temperature records are used. The phase difference between the various levels of the coherent signal, table 3.3, is also calculated.

These methods measure the phase difference of two slightly different fields. One is coherent with only the surface tide. The other includes all aspects of the field which are coherent over the length of the mooring.

The resultant phase differences $\Delta\phi_{ab}$ are plotted against $\int_a^b N(z)\,dz$ in figures 4.4 and 4.5. As expected, the two graphs are similar, the second, calculated from the directly measured coherence, being noisier. For comparison purposes, the same phase differences are plotted against the more conventional $\bar{N}_o \Delta z$, where Δz is the vertical distance between instruments and $\bar{N}_o$ is the mean buoyancy frequency over the array (figure 4.6 and 4.7). A least squares technique is used to fit the best straight lines for each graph. The slopes and correlation coefficients are listed in table 4.2. As can be seen in the graphs, the WKBJ approach gives a more homogeneous field. The various symbols, indicating measurements from different parts of the mooring, are brought much closer together using WKBJ than with the conventional. The correlation coefficients for WKBJ are also marginally better, though the 95% confidence limits indicate that only figure 4.7 is significantly different from the others.

The table of phases with depth (table 3.3), indicates that, in the coherent field, phase is propagating toward the surface, or energy is propagating down. This upward propagation of phase is also in the directly measured signal. Table 4.3 lists a few relevant phase differences with their confidence limits. The deeper instruments always lead the shallower. This phase difference can not be attributed to mooring motion, for that has been removed from the coherent signal. Nor can it be attributed to interferences among N_2, S_2 and M_2. Table 4.4 lists phases for high resolution coherences among the instruments. Even with the highest resolution, there are large phase differ-

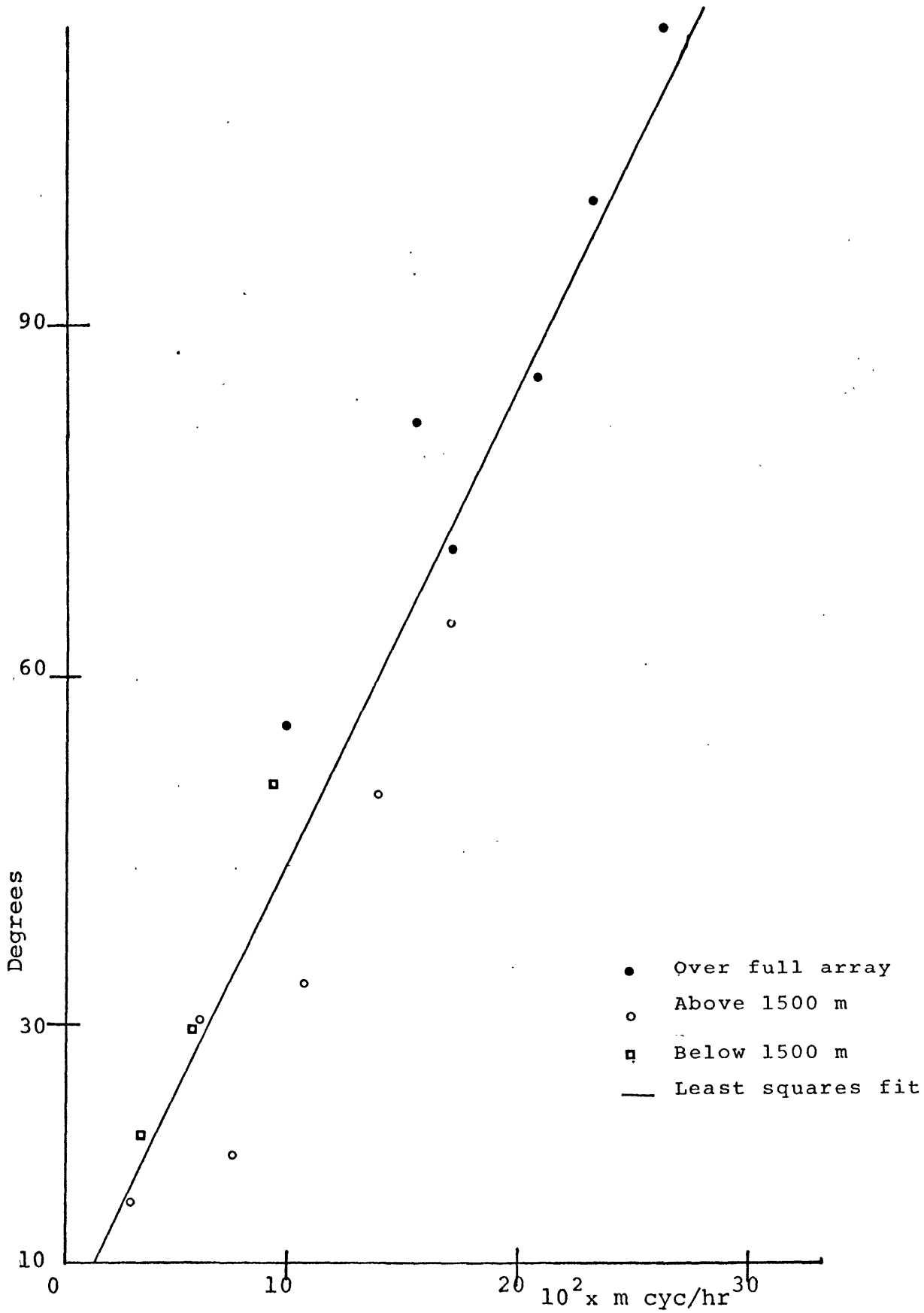

4.4 The phase change between instruments vs. the $\int N(z)dz$ between instruments for coherent Ups

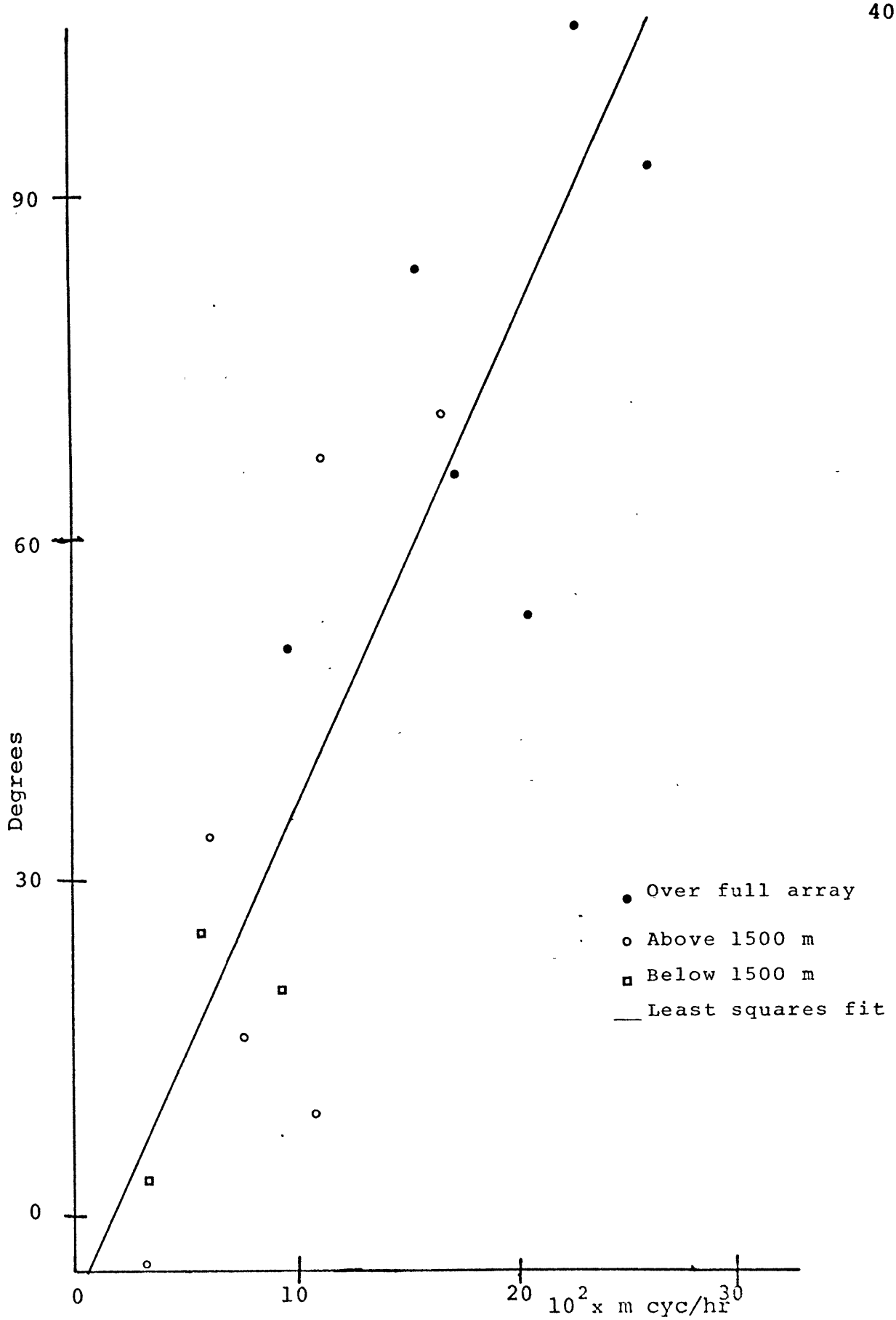

4.5 Phase change between instruments vs $\int N(z)dz$ between instruments for Ups

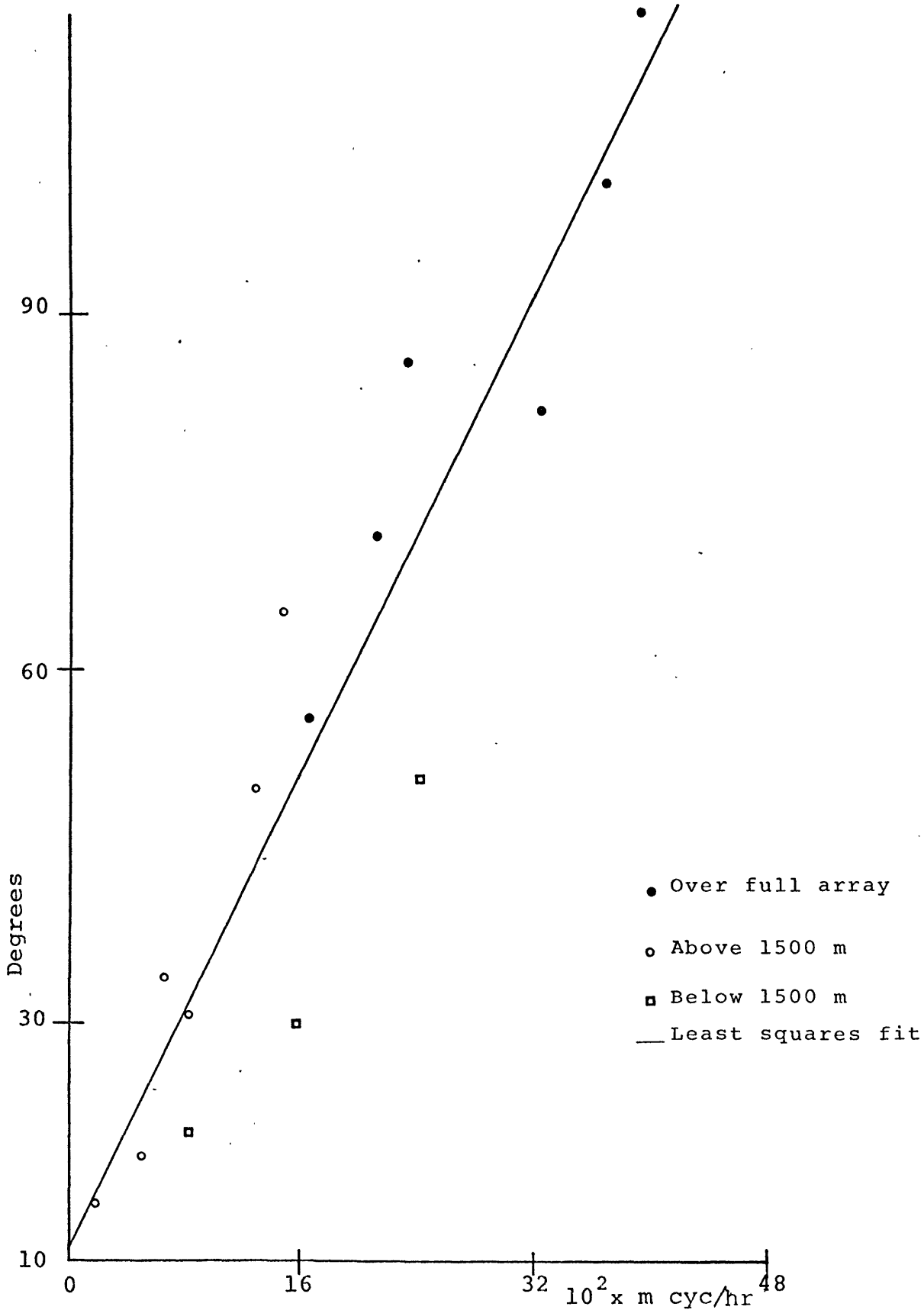

4.6 Phase change between instruments vs $N_o \Delta z$ between instruments for coherent Ups

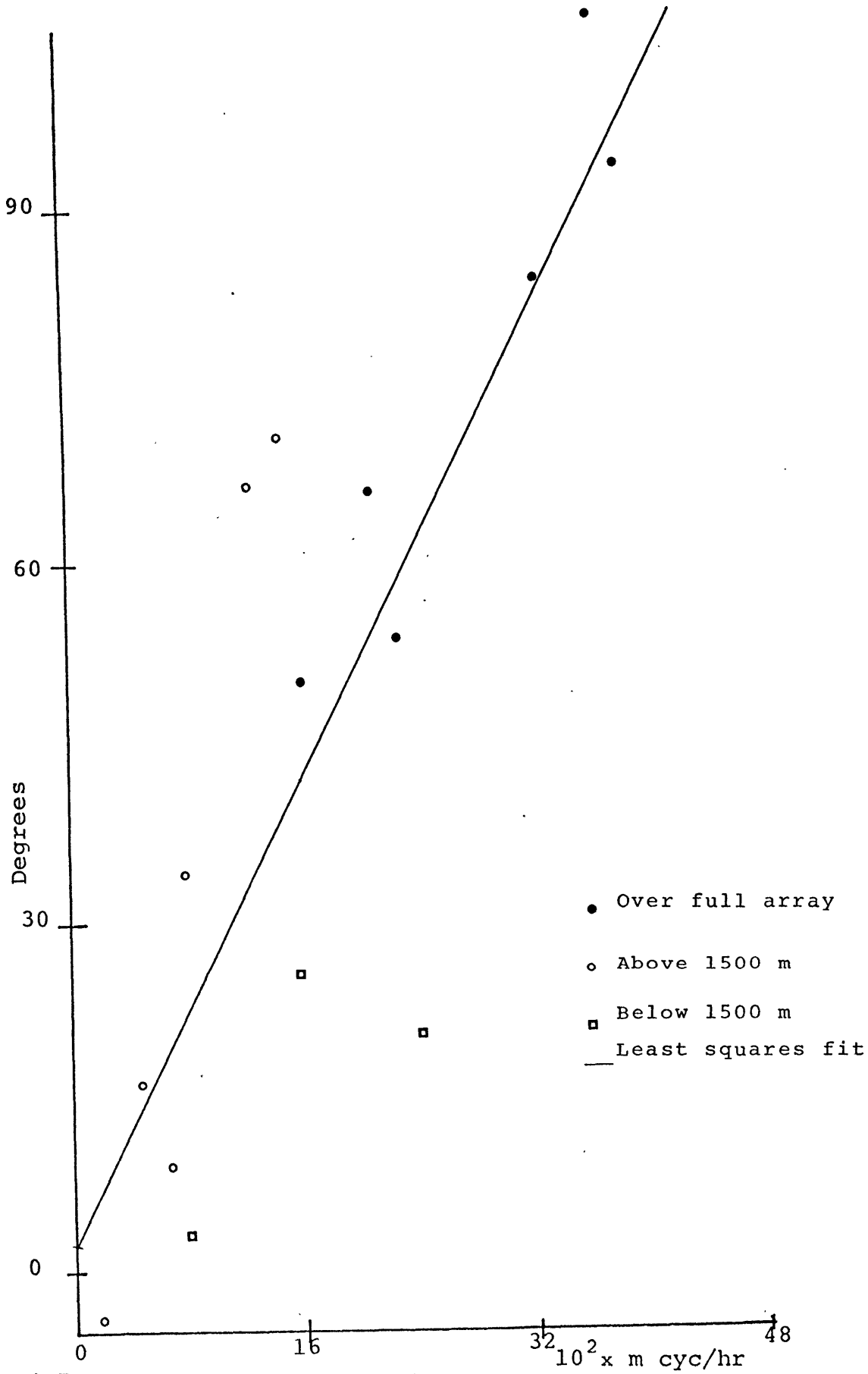

4.7 Phase change between instruments vs $N_o \Delta z$ between instruments for Ups

ences between the instruments.

A horizontal scale for this process can be calculated from the slope of figure 4.4.

$$K_H = \left[\frac{\Delta\phi_{ab}}{\int_a^b N(z)\,dz} \right] (\sigma^2 - f^2)^{\frac{1}{2}}$$

We calculate a wavelength of 128 km, with a range of 80 - 350 km, based on the 95% confidence limits for the value of the slope. This wavelength is of the same magnitude as that found by Hendry (1975) for the same area. His analysis was based on a modal decomposition similar to that presented later. It also compares favorably with scales found in subsequent analyses using maximum likelihood methods.

While it is possible to explain the observed phase changes with a (large) number of vertical modes, we believe that the simplest explanation is that vertical nodes are inappropriate. Rather a ray-like description of the internal semidiurnal tide is more plausible.

Table 4.1

Depth meters	East cm^2/sec^2	North cm^2/sec^2
620	9.2	14.0
724	9.9	13.1
1017	13.9	14.5
2044	7.7	3.6

Mean square current profile vs. depth

Table 4.2

Figure	Slope deg hr/m cyc	Correlation Coef.
4.4	4.20	.959
4.5	4.27	.880
4.6	3.99	.927
4.7	3.92	.825

Least squares estimate of slopes for Figures 4.4-4.7

Table 4.3

Instruments Pairs	Phase Difference	Confidence Band
6 - 15	106°	22°
6 - 12	67°	38°
6 - 14	66°	32°
10 - 15	84°	31°

Selected phase differences between instrument pairs

Table 4.4

Instrument Pairs	Resolution Hours	Phase Degrees
B6-B15	75	106
B6-B15	224.38	96
B6-B15	360*	92
B6-A14	75	66
B6-A14	224.38	86
B6-A14	360*	87

* This resolution separates S_2 from M_2

Phase stability as a function of resolution for selected MLM instrument pairs

5.0 WAVENUMBER SPECTRA

The investigation of the wavenumber spectra traditionally involves the use of conventional, or beamforming methods. These estimate the power spectra through a spatial fourier transform of the cross power spectral density matrix $f_{ij}(\sigma)$, calculated at a specific frequency from the data. The subscripts i, j represent the vector locations of sensor sites. An extensive discussion of standard techniques focused in the time domain may be found in Blackman and Tukey (1959). With the advent of fast Fourier transforms (FFT) (Cooley and Tukey, 1965), the brunt of analysis shifted into the frequency domaine, but the essential methods of statistical analysis remained the same.

With a limited data set, the above techniques have certain disadvantages. They all involve use of data independent window functions, which may permit strong spectral peaks to "leak" into adjacent wavenumber bands, thus inducing erroneous energy estimates. The minimum wavenumber which can be resolved by this method is the inverse of the largest separation between instruments.

Recently data adaptive methods have been introduced by Capon (1969). The maximum likelihood method (MLM), which can be derived in terms of a minimum variance estimator of the spectral components (Lacoss (1971)), is used below to estimate the wavenumber spectra of internal tides. This nonlinear method has a window function based on the data, as well as on the instrument array. When computing the power at a wavenumber k_o, this filter will pass undistorted a wave of that wavenumber,

while suppressing in a least squared sense, all waves of differing wavenumber. This minimizes spectral leakage. With MLM, we can resolve wavenumbers considerably below the minimum allowed by the conventional methods. This method is most effective for a few peaks embedded in background noise. As the information to be processed increases, or as the noise level rises, MLM approaches the effectiveness of the conventional method.

The cross-power spectral density matrix is

$$f_{ij}(\sigma) = \frac{1}{M} \sum_{m=1}^{M} \tilde{H}^{*}_{im}(\sigma)\ \tilde{H}_{jm}(\sigma)$$

where $H_{im}(\sigma)$ denotes the fourier transform of a signal measured by instrument i during a time period (or piece) m. The original time series is divided into M pieces.

The power estimate of the conventional method is

$$\hat{P}(\sigma,k) = \frac{1}{L} \sum_{j,i=1}^{L} w^{*}_{i} w_{j} f_{ij}(\sigma) e^{i\underset{\sim}{k}\cdot(\underset{\sim}{x}_i - \underset{\sim}{x}_j)} \tag{5.1}$$

where w denotes the window weights, L the total number of instruments, and $\underset{\sim}{x}_j$ the position of instrument j. The power estimate for the MLM is

$$\hat{P}(\sigma,k) = \left[\sum_{j,\ell=1}^{L} q_{j\ell}(\sigma) e^{i\underset{\sim}{k}\cdot(\underset{\sim}{x}_j - \underset{\sim}{x}_\ell)} \right]^{-1} \tag{5.2}$$

where $q_{j\ell}(\sigma)$ is the inverse of $f_{ij}(\sigma)$. Both the conventional and MLM will be used in subsequent analysis.

The conventional and high resolution methods assume only plane waves pass through the array. However, for ocean internal waves, k_z is not depth independent. From the dispersion relation

$$k_z^2(z) = \frac{N^2(z)-\sigma^2}{(\sigma^2-f^2)} k_H^2$$

Over the IWEX array, k_z varies between 30 and 180% of an average value. The effect of this variation and a method to accommodate it is discussed in the appendix. The essence of the method is to include the same variation of vertical wavenumber in the exponent of expressions (5.1) and (5.2) as is found in the input signal.

For internal tides, where $\sigma^2 << N^2$, the vertical wavenumber may be modeled as

$$k_z(z) = \pm N(z) \left(\frac{k_H^2}{(\sigma^2-f^2)} \right)^{1/2}$$

In a linear format

$$k_z(z_i) = \pm \left[1 + \frac{N(z_i)-\bar{N}}{\bar{N}} \right] \left[\frac{\bar{N}^2 k_H^2}{(\sigma^2-f^2)} \right]^{1/2} \qquad (5.3)$$

$$= \pm \left[1 + \frac{N(z_i)-\bar{N}}{\bar{N}} \right] k_{z_0}$$

where $\bar{N}$ is the average Brunt Väisälä frequency over the array. With the above scaling, k_z retains its relative magnitude. The exponent from expression 5.2 becomes

$$i \underset{\sim}{k}_H \cdot (\underset{\sim}{x}_j - \underset{\sim}{x}_\ell) + i\, k_z(z_j) \cdot z_j - i\, k_z(z_\ell) \cdot z_\ell. \qquad (5.4)$$

Using seven instruments (A4, B6, C10, A12, B14, B15, C15) the cross spectral matrix $f_{ij}(\sigma)$ is computed. Wavenumber spectra are calculated for two resolutions ($\Delta k = \frac{2\pi}{2500}, \frac{2\pi}{5000}\ m^{-1}$) on a 51 × 51 grid. The highest wavenumber which can be calculated is 25 times the resolution. Both MLM and the conventional, with weights w equal to one, are used. Given that the aperture of the array is 2500 meters, the conventional method can only strictly apply to the first ($2\pi/2500$) resolution. The spectra are calculated for each resolution with and without scaling the vertical wavenumber by the Brunt Väisälä frequency. In all cases, the unscaled array was much noisier, but had similar general features. Henceforth, only the scaled array will be discussed.

Because the coherence matrix is normalized for these calculations, there is no way of determining absolute power in the wavenumber spectrum. The MLM does conserve peak height (Lacoss, 1971), therefore the spectral shape may be determined with each method.

In figure 5.1, a section of the MLM "beam pattern" in the $k_x k_z$ plane, centered on $k_x = k_z = 0$, for a signal to noise ratio of one and a resolution of $\frac{2\pi}{2500}\ m^{-1}$, is reproduced. For a discussion of conventional and MLM beam patterns, see the appendix. The units are power, in decibels down from the largest peak (of value zero). Note the symmetry in k_z. The major peak is found at o, o, as expected. The leakage into

other wavenumbers is minimal. A spurious peak is found at $k_z = \pm 5$, $k_x = 0$. Other minor peaks are scattered over the grid. This beam pattern was chosen because the average background noise is of the same level as that found in the data. The conventional beam pattern is similar, but much noisier (figure 5.2).

In figure 5.3, a section from the MLM realization of the power spectrum for the $k_x k_z$ plane is reproduced. Energy is concentrated in $k_z = 0, +1, +2$; $k_x = 0$. Lower energies are found in $k_z = -1, -2$; $k_x = 0$. Phase is propagating upward. With fourteen degrees of freedom, the numbers between 0 and 3 are statistically equivalent. The peak at $k_z = 1$, $k_x = 0$ is significantly different from its partner at $k_z = -1$, $k_x = 0$. The concentration at $k_z = 2$ is not. This implies energy, with a maximum scale of 2500 m, is propagating down. The other energy peaks ($k_z = 10$, $k_x = 0$; $k_z = 14$, $k_x = 1$) are spurious. They are also found in the conventional beam pattern.

The slight spreading of energy into k_x around $k_z = 0$ is an artifact of the ray nature of the field. According to the dispersion relation, energy propagates along a cone in k_z, k_H space. The straight lines drawn in figures 5.3 and 5.5 are the intersection of this cone with the $k_x k_z$ plane. In tests of the response of this method to artificial data simulating cones, energy spread into ellipses rather than remaining in rays. Thus, neither method can resolve intersecting cones. This is not

Figure 5.1

Beam Pattern MLM

2500 m^{-1} resolution k_x k_z plane

8	9	9	9	7	8	9
9	8	7	9	9	9	9
9	6	7	8	8	7	9
9	7	9	9	5	9	9
8	7	8	8	9	9	8
9	8	9	8	6	9	9
9	9	9	7	9	9	8
9	7	9	9	9	7	8
8	8	9	8	8	9	9
8	8	9	8	9	9	8
7	8	9	9	8	9	9
9	9	8	7	9	9	8
9	8	8	9	9	7	9
9	8	9	9	7	9	9
8	8	8	9	9	9	8
8	7	9	9	6	9	9
9	9	9	6	8	9	7
9	8	8	9	9	8	7
8	8	9	8	7	9	9
8	8	9	8	9	9	7
7	7	9	8	8	9	9
7	9	8	(0)	8	9	7
9	9	8	8	9	7	7
7	9	9	8	9	8	8
9	9	7	8	9	8	8
7	8	9	9	8	8	9
7	9	8	6	9	9	9
9	9	6	9	9	7	8
8	9	9	9	8	8	8
9	9	7	9	9	8	9
9	7	9	9	8	8	9
8	9	9	7	8	9	9
9	9	8	9	9	8	7
8	9	9	8	9	8	8
9	9	8	8	9	8	8
8	7	9	9	9	7	9
8	9	9	7	9	9	9
9	9	6	8	9	8	9
8	9	9	8	8	7	8
9	9	5	9	9	7	9
9	7	8	8	7	6	9
9	9	9	9	7	8	9
9	8	7	9	9	9	8

Power in NE Quadrant = 56.26

Power in NW Quadrant = 56.71

Power in SW Quadrant = 56.26

Power in SE Quadrant = 56.71

Total Power = 225.93

$$\Delta k_x = \Delta k_z = \frac{2\pi}{2500}\ m^{-1}$$

$k_x = k_y = 0$ is circled

Figure 5.2

Conventional Beam Pattern

2500 m^{-1} resolution k_x k_z plane

6	11	11	26	4	8	13
14	5	3	9	11	16	10
12	3	4	9	6	3	22
21	5	11	13	2	9	15
6	5	6	8	9	11	6
10	5	16	8	2	20	14
15	13	11	4	14	15	5
11	4	9	20	15	5	9
8	9	24	8	5	15	15
6	7	9	9	17	11	8
4	7	12	11	5	11	23
11	14	8	4	18	25	8
24	7	5	21	15	4	11
10	9	17	14	3	11	16
9	8	6	11	10	10	7
7	5	18	10	2	15	12
13	22	16	3	7	9	4
14	5	9	16	12	9	4
8	8	17	7	5	25	12
5	7	12	5	11	27	4
3	3	10	7	5	11	11
4	11	8	(0)	8	11	4
11	11	5	7	10	3	3
4	27	11	5	12	7	5
12	25	5	7	17	8	8
4	9	12	16	9	5	14
4	9	7	3	16	22	13
12	15	2	10	18	5	7
7	10	10	11	6	8	9
16	11	3	14	17	9	10
11	4	15	21	5	7	24
8	25	18	4	8	14	11
23	11	5	11	12	7	4
8	11	17	9	9	7	6
15	15	5	8	24	9	8
9	5	15	20	9	4	11
5	15	14	4	11	13	15
14	20	2	8	16	5	10
6	11	9	8	6	5	6
15	9	2	13	11	5	21
22	3	6	9	4	3	12
10	16	11	9	3	5	14
13	8	4	26	11	11	6

Power in NE Quadrant = 92.83

Power in NW Quadrant = 94.09

Power in SW Quadrant = 92.83

Power in SE Quadrant = 94.09

Total Power = 373.84

$$\Delta k_x = \Delta k_z = \frac{2\pi}{2500}\ m^{-1}$$

$k_x = k_y = 0$ is circled

Figure 5.3

MLM Wavenumber Spectra

2500 m^{-1} resolution k_x k_z plane

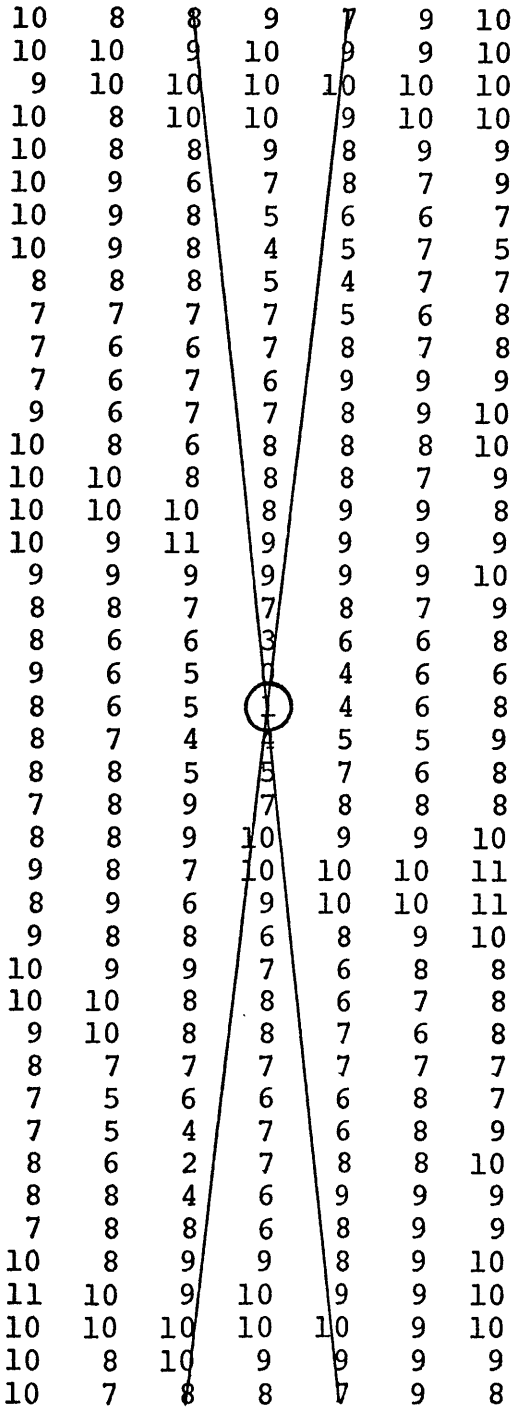

Power in NE Quearant = 20.03

Power in NW Quadrant = 19.96

Power in SW Quadrant = 20.27

Power in SE Quadrant = 20.11

Total Power = 80.38

$$\Delta k_x = \Delta k_z = \frac{2\pi}{2500}\ m^{-1}$$

$k_x = k_y = 0$ is circled

—— is characteristic ray path for tidal frequency

Figure 5.4

Conventional Wavenumber Spectra

2500 m^{-1} resolution k_x k_z plane

8	6	6	7	5	6	9
5	6	7	9	6	5	10
5	3	10	10	6	5	10
9	2	9	10	6	5	8
10	3	7	8	6	8	7
10	4	6	8	4	8	9
6	7	5	4	5	5	5
4	10	7	2	7	6	2
5	7	9	3	5	9	3
7	7	4	8	5	5	6
5	8	3	5	8	5	5
4	4	6	3	6	8	3
7	3	6	5	4	7	5
10	6	4	8	5	4	7
8	8	6	8	5	4	8
8	5	8	8	5	3	7
8	5	9	7	7	3	4
7	5	9	6	6	6	4
7	5	5	6	5	7	8
5	6	4	2	8	6	6
3	6	7	0	5	7	3
5	5	6	1	2	4	5
8	7	3	3	3	1	9
5	7	4	6	7	2	6
4	3	7	6	8	4	5
6	2	4	9	8	4	6
6	5	2	7	10	4	7
5	7	3	5	8	6	8
5	8	4	4	6	8	10
4	8	6	3	4	9	8
4	6	8	4	1	8	8
4	6	6	9	1	4	9
3	8	6	6	5	4	4
2	5	7	4	8	8	2
4	3	2	7	6	7	5
6	6	0	7	8	4	8
6	8	2	3	9	5	6
7	5	7	4	5	9	6
8	5	8	8	5	7	8
5	6	8	10	5	6	10
5	5	10	10	5	6	10
7	4	9	8	6	6	8
7	5	9	5	6	8	6

Power in NE Quadrant = 93.70

Power in NW Quadrant = 95.36

Power in SW Quadrant = 95.07

Power in SE Quadrant = 94.80

Total Power = 378.92

$$\Delta k_x = \Delta k_z = \frac{2\pi}{2500}\ m^{-1}$$

$k_x = k_y = 0$ is circled

—— is characteristic ray path for tidal frequency

obviously true from analysis of the tides as horizontal wavenumbers are too small to be resolved by the IWEX array anyway.

A section of the conventional realization of the power spectra is shown in figure 5.4. Note upward phase propagation is also indicated. With 26 degrees of freedom available to the conventional method, the downward energy propagation is more significant than for the MLM. There is a statistically significant difference for $k_z = 2$. It may not be real, for leakage from the peak at one may cause this additional asymmetry.

In both methods, there is no significant energy found in vertical wavelengths smaller than 1250 meters. The peak found on the $k_x k_z$ plane at $k_x = -1$, $k_z = -14$ is spurious. It is near a strong projection found in the conventional beam pattern ($k_x = -2$, $k_z = -14$). This peak was not found in any other cuts through k space. These other cuts were in the k_z , k_y and k_z, $\sqrt{k_x^2 + k_y^2} \mid k_x = k_y$ planes. The patterns were very similar to the $k_z k_x$ realization. As was mentioned above, the array was too small to resolve horizontal propagation.

To investigate the spectrum in finer detail, the resolution was doubled ($2\pi/5000$ m^{-1}). The MLM spectrum is depicted in figure 5.5. The beam pattern is similar to that for 2500 m^{-1} . No spurious peaks appear less than ten grid points from the origin on the $k_x = 0$ axis. As the field in figure 5.5 is similar to other vertical cuts through k space, only the $k_z k_x$ cut will be discussed.

Figure 5.5

MLM Wavenumber Spectra

k_x k_z plane, 5000 m^{-1} resolution

10	6	9	7	11	9	12
10	7	10	6	10	9	12
10	7	10	6	10	9	12
10	7	11	7	10	8	11
10	7	11	8	11	8	10
10	6	11	8	11	8	10
11	6	11	9	11	8	10
11	8	11	8	11	9	11
12	9	12	8	11	9	11
12	11	12	8	11	9	11
12	11	12	9	11	9	11
12	11	12	9	12	9	11
12	10	12	9	12	9	11
11	9	11	9	11	9	11
11	8	11	8	11	8	11
10	7	10	7	10	8	10
10	6	10	5	10	7	10
10	6	9	3	9	6	9
10	6	9	2	9	5	9
10	5	9	0	9	5	9
10	5	9	0	8	4	9
10	5	10	1	9	4	9
9	5	10	3	9	4	8
9	4	9	4	10	5	8
9	4	9	5	11	6	9
10	5	9	5	11	7	10
11	7	9	6	11	8	11
11	9	10	7	11	8	11
11	9	11	8	11	9	12
11	9	12	10	12	9	12
11	9	11	10	12	10	12
11	8	11	11	12	10	12
11	6	11	10	12	10	12
11	6	11	9	11	10	12
11	7	11	8	11	9	11
11	8	11	6	10	8	10
11	9	11	6	10	7	9
11	9	11	7	11	6	9
11	9	11	8	11	6	9
11	9	11	8	11	6	9
11	9	11	8	11	7	10
11	9	11	8	11	7	10
10	8	11	8	11	7	10

Power in NE Quadrant = 20.29
Power in NW Quadrant = 20.51
Power in SW Quadrant = 20.68
Power in SE Quadrant = 20.91
Total Power = 82.39

$\Delta k_x = \Delta k_z = \frac{2\pi}{5000}\ m^{-1}$

$k_x = k_y = 0$ is circled

—— is characteristic ray path for tidal frequency

Energy is again concentrated in scales larger than 1250 meters and phase is propagating upward. For λ_z = 5000 m and 1670 m, the vertical asymmetry is bordering on significance. For λ_z = 2500 m , it is significant

The horizontal scales for phase propagating toward the surface found by the WKBJ approximation in section four can be related to vertical scales through the dispersion relation

$$\lambda_z = \frac{(\sigma^2-f^2)^{\frac{1}{2}}}{\bar{N}} \lambda_H$$

where $\bar{N}$ is the average Brunt Väisälä frequency used to scale k_z . For λ_H = 128 km ,

$$\lambda_z = 5.3 \text{ km}$$

with a range of 3.4 - 14.9 km. This agrees with the range found by MLM. In formula 4.1, the slight spread in wavenumber found with MLM would slightly blur the linear relation. This would account for some of the scatter found in figures 4.4 and 4.5.

6.0 MODAL DECOMPOSITION

Traditionally internal tides are analyzed by decomposing the field into normal modes. The details of this technique are well known. Magaard and McKee (1973), in their analysis of currents at site D in the northwestern Atlantic, and Ross Hendry (1975) present a comprehensive treatment of modal analysis.

A modal decomposition presupposes the absence of vertically propagating waves. Until recently, there has been no reliable method to measure vertical propagation characteristics of the internal tidal field. The assumption was made that, far from continental margins, energy propagated horizontally. Vertical propagation would change the phase characteristics of the field, but it would not necessarily preclude a "good" normal mode fit. Some criteria for a good fit are given in appendix A.4.

With an infinite set of normal modes, any well-behaved field can be fit absolutely. More realistically, only a limited set of modes, which are chosen with regard to the measured vertical resolution, can reliably be fit to the data. Figure 6.1 depicts the shapes of the first five Up, or isotherm displacement, modes, together with the IWEX instrument sites. To eliminate aliasing problems, an instrument should be placed between each zero crossing. Failing this, there should be a high density of instruments where a significant difference in curvature exists between unresolved modes.

Figure 6.1 illustrates that the Up and coherent isotherm displacement signal (PT) (Table 3.3) will give the most reliable decomposition. For currents, there are fewer instrument sites

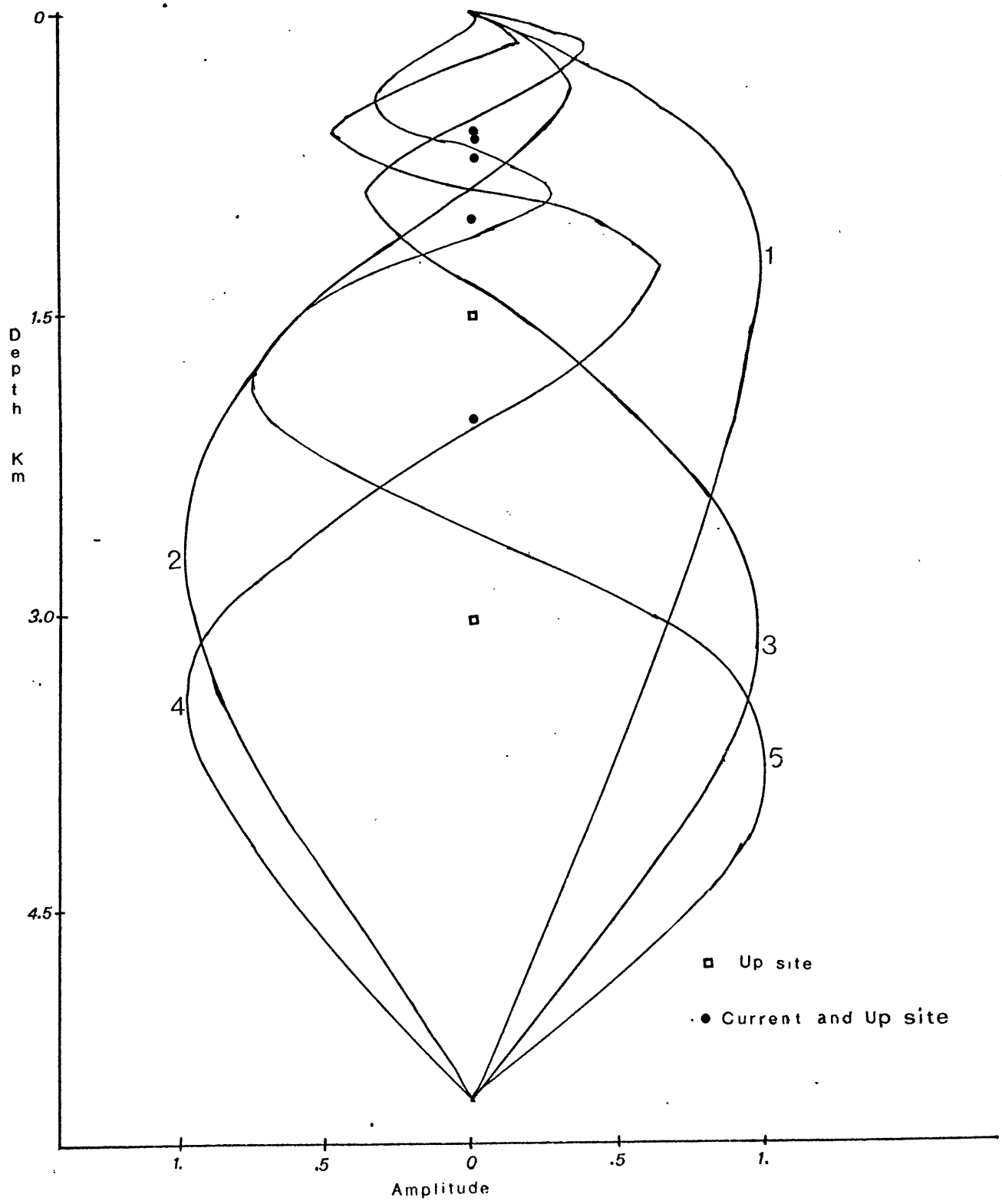

6.1 Isotherm displacement modes. Instrument sites are depicted.

and greater aliasing problems. The current modal shapes are proportional to the vertical derivative of the Up modes. They have one additional zero crossing and therefore need greater instrument resolution. The barotropic tide, mode zero, must also be included in each set of modes, thereby decreasing the number of baroclinic horizontal current components which can be fit.

Maximum likelihood calculations indicate that energy is contained in large vertical scales. Modes one through five span these scales. They comprise the set of modes used to decompose the internal tidal field.

For all combinations, the available modes are fit, in a least squares sense, to the seven Up and six PT data points in sets of three, two, and one. The details of this process are described in the appendix. Modes zero through five are fit to the five current measurements in sets of three and two. Mode zero is included in each current decomposition. The criteria in appendix A.4 are used to determine which set of modes best fits the data. For an acceptable decomposition to occur, the criteria should not only be satisfied, but the chosen set of modes should be unambiguously differentiated from all others.

To study temporal variation, the records are divided into five segments of equal length. The real and imaginary components of the signal for each segment are formed from an average

of five, overlapped, hanned, seventy-five hour pieces. At each level, these components are averaged across the array. For most levels, a shift in average phase occurred between segments three and four (see figure 6.2). To obtain higher statistical reliability, the signal components for the first three segments are averaged into U<3>, N<3>, and E<3>. Thes span the first 3/5 of the record. The last two sentences are also averaged (U<2>, E<2>, N<2>). An average across all five segments determines the total signal (U<5>, E<5>, N<5>).

The Up and PT signals are decomposed into modes. Using the confidence tests, PT fit best, with U<2>, U<5>, and U<3> following respectively. The amplitude, phase, and vertically integrated energy of these decompositions are listed in Table 6.1. Low modes dominate the energy spectrum, with mode one appearing strongly in all signals.

The differing decomposition and energy levels of U<3> and U<2> indicate that the field varies with time. Even though a modal decomposition may not be the best method of analyzing the field, as implied in sections four and five, changing characteristics of the internal tidal band will be reflected in the decomposition. The last 2/5 of the record, U<2>, shows a more highly structured, more energetic field. This is consistent with the temporal variation of energy illustrated by figure 2.4. It is not surprising that U<5> shows the least energy. The component averaging process tends to cancel temporal variations.

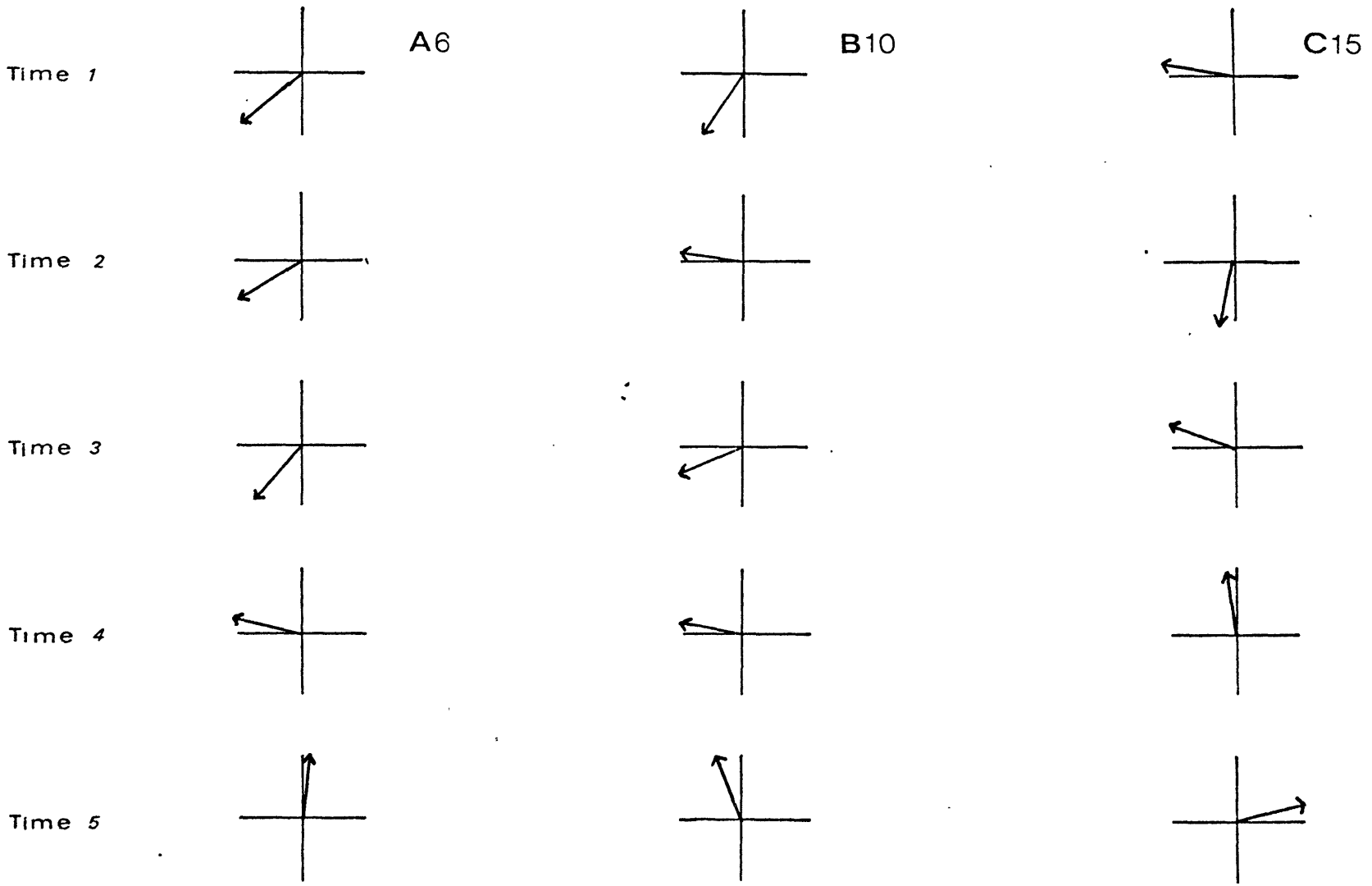

Figure 6.2 Phase of instrument with time

TABLE 6.1

MODAL AMPLITUDE AND INTEGRATED ENERGY DENSITY

Signal Type	MODE 1		MODE 2		MODE 3	
	Amplitude* and Phase**	Energy 10^{+4} ergs/cm^2	Amplitude and Phase	Energy 10^{+4} ergs/cm^2	Amplitude and Phase	Energy 10^{+4} ergs/cm^2
PT	$3.94e^{i37°}$	6.99	$5.7e^{i113°}$	4.22	***	***
U<5>	$2.78e^{i65°}$	3.48	***	***	$3.71e^{i67°}$	2.41
U<3>	$4.04e^{i141°}$	7.33	$4.40e^{-i65°}$	2.52	***	***
U<2>	$5.12e^{i108°}$	11.75	***	***	$5.68e^{i26°}$	5.65

* Amplitude in dimentionless units.

** Phase of PT is with respect to tidal signal.
Phase of U<x> is with respect to time t = 0 on November 11, 1973 at 16:36 o'clock.

*** The energy in this mode could not be reliably estimated.

The coherent temperature field, PT, has more energy and a lower modal decomposition than U<5>. It measures a slightly different field, one which is coherent with the surface tides. PT measures a cleaner field, as shown by its better confidence tests, for that portion of the internal tides which is Doppler shifted and scattered by interactions with the surrounding medium is removed. Higher modes, with more vertical shear, interact more strongly with the surrounding medium. The higher modal content of U<5> illustrates this since the shifted portion of the field is not necessarily averaged out. The lower energy levels of U<5> imply that the incoherent field is more random in time. The total energy measured by the modal decomposition is consistant with the scales found in Section three.

The currents were decomposed into normal modes. No decomposition passed the confidence tests.

7.0 CONCLUSION

This report analyzes the semi-diurnal tidal field measured during IWEX. In a similar region of the northwestern Atlantic, Hendry (1975) studied internal tides, based on data from a long range, large horizontal scale experiment (MODE). Only that portion of the field coherent with the equilibrium tide was analyzed. With longer records, he was able to resolve the N_2, S_2, and M_2 frequency bands. The structure of the temperature and current field for N_2 and S_2 was found to be very similar to that of M_2, only not as coherent with the equilibirum tide, suggesting the N_2 and S_2 frequency bands were dominated by a Doppler-shifted M_2 field. The energy in M_2 was three times that of N_2 and S_2.

The depth integrated energy was about four times that measured by the IWEX array. IWEX took place near the beginning of MODE. The temperature time series from MODE places IWEX just before a front, which suggests a general rise in energy throughout the region. The increase in energy over the last half of the IWEX experiment (figure 2.4) is consistent with this.

Hendry decomposed the M_2 isotherms into normal modes. Most of the energy was concentrated in mode one. At the central mooring, mode three was the next most energetic, with 12% of the energy. The internal tides were found to be propagating toward the southwest. No estimate of the vertical propagation of energy was made.

For IWEX, energy in the semidiurnal tidal band was found to be propagating toward the sea floor, with vertical scales larger than 1.7 kilometers. The depth integrated energy of that portion of the field coherent with the surface tide was estimated to be $1. \times 10^5 ergs/cm^2$. Due to the short record length, M_2 could not be resolved, but Hendry indicates that the tidal band is dominated by the M_2 frequency. This is consistent with the IWEX results that the coherence characteristics of the field are relatively independent of resolution (Table 2.2 and Table 4.4).

To facilitate comparison of our results with Hendry's, the field was decomposed into normal modes, even though evidence indicated that a modal analysis does not apply. The PT signal of section six is most analogous to Hendry's data, for it is coherent with the surface tide. Despite the large phase change with depth, mode one (whose phase is constant with depth) carried the largest energy, 62% of the total. Mode two carried much of the remainder.

Table 7.1 lists the magnitudes of the coherence, with depth, for the Ups. The coherence maximum is between 730 and 1020 meters. If the noise is defined to be that portion of the signal which is not coherent with the surface tide, then the coherence squared is a measure of the signal to noise ratio. Under the assumption that the noise power is equally distributed over the water column, the coherence should maximize at the same level as the dominate mode maximizes. Mode one reaches a maximum at 1250 meters. Unfortunately there are

no measurements at that depth, but the coherence field does not appear symmetric near this value. Interference from mode two could account for this, but above 1700 meters its amplitude is small. The asymmetry is measurable, but not statistically significant. It suggests that this simple model may not account for the coherence field.

Because significant energy appears on both positive and negative vertical wavenumbers, figure 5.1, it is possible to fit modes to the internal tidal field (Appendix A.5). It is not surprising that the general scales found by MLM and a modal decomposition are compatible. Energy found on the first three modes, with vertical scales

$$\lambda z_1 = 6.9 \text{ km}$$

$$\lambda z_2 = 3.0 \text{ km}$$

$$\lambda z_3 = 2.4 \text{ km}$$

would appear in grid points $k_z = 0, \pm 1, \pm 2$ of figure 5.5. The scale for mode one ($k_z = 0, \pm 1$) also dominates the MLM realization of the power spectrum. The energy in $k_z = +3, +4$ does not appear in the modal decomposition, for the energy in the paired scale ($k_z = -3, -4$) is low.

Even though it is possible to explain the observed phase changes of the field through a modal fit, the most consistent explanation is that normal modes are inappropriate. The large phase changes over the IWEX mooring are real. They cannot be

explained by mooring motion or by beating among M_2, S_2, and N_2. Hendry does not find such large phase changes at his central mooring, but mooring three shows significant phase changes with depth.

Both WKBJ and MLM support a ray-like description of the field. The energy propagating downward implies that the internal tide is generated at least 115 kilometers from the IWEX area. Given an average Brunt-Väisälä frequency of .0028 radians per second and an average ocean depth of five kilometers, an internal tidal wave packet would progress 115 kilometers horizontally as it traversed the water column. This precludes any nearby bottom generation of the field, for then energy would be found to propagate upward.

Internal tides may be generated on steep slopes, such as continental margins (Rattray, et al. (1969)) or on abyssal bottom relief, such as the mid-Atlantic ridge. Hendry found internal tides in this region propagating toward the southwest. The generation region could be the continental slope, seven to eight hundred kilometers away. For this to occur the internal tides would have to reflect three times from the surface boundaries, a not unreasonable criteria.

Far field generation is consistent with the scales found in the IWEX region. Near the source, a broad range of vertical scales might be generated, with much shorter scales than found at the IWEX tri-moor. For equal amplitudes, these shorter scales have higher shear, and therefore, a greater dissipative rate. They damp out much sooner than the longer scales.

TABLE 7.1

The Magnitude of the Coherence of Selected Instruments with the Surface Tide

Instrument	Depth Meters	Coherence Magnitude*
C3	607	.55
A4	610	.57
A6	731	.74
A9	1020	.74
C9	1020	.70
A10	1023	.75
A12	1530	.62
A14	2050	.50
C14	2050	.60
A15	3050	.55
C15	3050	.53

*95% confidence level for zero significance is .51.

REFERENCES

Blackman, R.B. and J.W. Tukey, The Measurement of Power Spectra from the Point of View of Communications Engineering, New York, Dover, 190 pp. 1959

Briscoe, M.G., Preliminary results from the tri-moored internal wave experiment (IWEX), Journal of Geophysical Research, 80, 1975b

Cartwright, D.E., A unified analysis of tides and surges round north and east Britain, Phil. Trans. R. Soc. London, A1134, 1-55 1966

Capon, J., High-resolution frequency-wavenumber spectrum analysis, Proceedings of the IEEE, 57, No.8, 1408-1418 August 1969

Capon, J., Applications of detection and estimation theory to large array seismology, Proceedings of the IEEE, 58, No.5, 760-770 May 1970

Cooley, J.W. and J.W. Tukey, An algorithm for the machine calculation of complex Fourier series, Mathematics of Computation, 19, 297-301 1965

Defant, A., Internal waves and their stability conditions, Arch. Met. Geophys., Bioklimat., Al, 39-61 1949

Hendry, R., The generation, energetics and propagation of internal tides in the western North Atlantic Ocean, PhD thesis, M.I.T., Cambridge, Mass. June 1975

Lacoss, R.T., Data adaptive spectral analysis methods, Geophysics, 36, No.4, 661-675 August 1971

Maeda, A., Phase velocity of semi-diurnal internal waves at ocean weather station T, J.Ocean. Soc. Japan, 27, No.4, 163-174 August 1971

Magaard, L. and W.D. McKee, Semi-diurnal tidal currents at 'Site D', Deep-Sea Res., 20, 997-1009 1973

Munk, W., and N. Phillips, Coherence and band structure of inertial motion in the sea, Rev. Geophys., 6, 447-472 1968

Nuttall, A., Spectral estimation by means of overlapped fast Fourier transform processing of windowed data, NUSC Report No.4169, October 1971

Phillips, O.M., Dynamics of the Upper Ocean, Cambridge Univ. Press, 261 pp., 1966

Rattray, M., Jr., J.G. Dworski, and P.E. Kovala, Generation of long internal waves at the continental slope, Deep-Sea Res., SUPP.16, 179-195 1969

Reid, J.L. Jr., Observations of internal tides in October 1950, Trans. Am. Geophys. Union, 37, No.3, 1956

Wunsch, C., Internal tides in the ocean, Rev. Geophys. Space Phys., (in press) 1975a

Wunsch, C., and J. Dahlen, A moored temperature and pressure recorder, Deep-Sea Res., 21, 145-154 1974

Zetler, B.D., Radiational ocean tides along the coasts of the United States, J. Phys. Oceanogr., 1, 34-38 1971

Zetler, B., W. Munk, H. Mofjeld, W. Brown, and F. Dormer, MODE Tides. (Submitted to J. Phys. Oceanogr.) 1975

APPENDIX A.1 WKBJ SCALING

The WKB solution to the equation

$$\left[\frac{d^2}{dz^2} + \frac{N^2(z)\ k_H^2}{(\sigma^2 - f^2)}\right] W(z) = 0$$

is

$$W(z) \simeq \frac{(\sigma^2 - f^2)^{\frac{1}{4}}}{N^{\frac{1}{2}}(z)\ k_H^{\frac{1}{2}}}\ e^{\pm i \frac{k_H}{(\sigma^2 - f^2)^{\frac{1}{2}}} \int N(z)dz}$$

with the condition that

$$\frac{N(z)\ k_H}{(\sigma^2 - f^2)^{\frac{1}{2}}} >> \frac{(N(z))'}{N(z)}$$

The above condition is the usual statement that the vertical scales of the field ($\frac{(\sigma^2 - f^2)^{\frac{1}{2}}}{N(z)\ k_H} \simeq \frac{\lambda_z}{2\pi}$) are less than the vertical scales of the medium.

The phase change with depth goes as the integral of the Väisälä frequency. The vertical velocity, or isotherm deflection, scales as $N^{-\frac{1}{2}}(z)$. Therefore, $N(z)W^2(z)$ or $N(z)Up^2$ should be constant with depth.

Appendix A.2 Beam Patterns

In the compilation of a wavenumber power spectrum, the beam pattern is convolved with the true spectrum. It is necessary to inspect this beam pattern, since, from an analysis of its structure in k space, one can predict where energy from strong peaks will leak. This allows one to discriminate between real and spurious peaks.

The beam pattern of the conventional technique is formed from $|B(k)|^2$, where

$$B(k) = \frac{1}{L} \sum_{j=1}^{L} e^{i \underset{\sim}{k} \cdot \underset{\sim}{x}_j} \qquad \text{(A.2.1)}$$

This beam pattern is equivalent to passing a wave of zero wavenumber through the array. Note the pattern depends only on the instrument positions.

For MLM, the beam pattern, $|B(k)|^2$ is derived by Capon (1970).

$$B(\sigma, k, k_o) = \sum_{j=1}^{L} A_j (\sigma, k_o) e^{i(\underset{\sim}{k}-\underset{\sim}{k}_o) \cdot \underset{\sim}{x}_j} \qquad \text{(A.2.2)}$$

where

$$A_j(\sigma, k_o) = \frac{\sum_{k=1}^{L} q_{jk}(\sigma)\, e^{i\underset{\sim}{k}_o \cdot (\underset{\sim}{x}_j - \underset{\sim}{x}_k)}}{\sum_{j,k=1}^{L} q_{jk}(\sigma) e^{i\underset{\sim}{k}_o (\underset{\sim}{x}_j - \underset{\sim}{x}_k)}} \qquad \text{(A.2.3)}$$

$\underset{\sim}{k}_o$ is the specific wavenumber at which the power density is being estimated. Through the q_{jk}'s this becomes a non-linear data dependent filter. Unlike the conventional pattern, it changes for each $\underset{\sim}{k}_o$ and for each data set processed. As the signal to noise ratio goes to zero, $f_{ij} = q_{ij}$ = real, unitary matrix. Then the above beam pattern approaches the conventional.

The MLM beam pattern is more difficult to interpret than the conventional. Not only does it change for each wavenumber, but it suppresses peaks, proportional to their strength, off $\underset{\sim}{k}_o$. Since the true peaks of the spectrum are unknown, the beam pattern does not show how energy leaks from other spectral peaks. Fortunately we can create a "beam pattern' for MLM that imparts information similar to that given by the conventional. The MLM is data dependent. Therefore an artificial signal is created similar to the spectrum expected from the data.

An initial look at the IWEX data indicated that the power in the internal tides is limited to a few low wavenumbers. Under the assumption that the "beam pattern" does not change markedly for a small shift in wavenumber, the spectrum is modeled as a single wave of zero wavenumber plus white noise. With the noise to signal ratio ranging from zero to two, this signal was processed with the MLM filter. When the noise increases, energy appears at wavenumbers other than zero. As expected, the peaks in the MLM beam pattern correspond to those most significant in the conventional, though their number, width and relative energies are much less.

In computing the MLM beam pattern for an array of many instruments and of limited duration, consideration must be given to which instruments are to be included in the computation of $q_{ij}(\sigma)$. The minimum number of instruments which give sufficient resolution should be chosen. From Capon (1970), the number of degrees of freedom available to the processor is $2(M - L + 1)$. Instruments A4, B6, C10, A12, B14, B15, and C15 were used in the decomposition. This pattern spanned the largest spatial separations, while providing sufficient resolution for the calculation of high wavenumbers. The beam pattern (Fig. 5.1) for this array has no significant peaks near zero wavenumber.

The power spectrum was computed for two dimentional slices through the three dimensional wavenumber space. $P(k_x k_y | k_z = 0)$, $P(k_x, k_z | k_y = 0)$, $P(k_y, k_z | k_x = 0)$ and $P(k_z, k_H = \sqrt{k_x^2 + k_y^2} | k_x = k_y)$ were the main slices calculated. For all cuts, the power in each quadrant was distributed approximately symetrically. Figures 5.1 and 5.2 show two such distributions.

Appendix A.3 Conventional and MLM sensitivity to depth dependent wavenumbers

To investigate the sensitivity of the conventional and MLM methods to a variable wavenumber, the power spectral matrix was derived for a signal

$$S = \int_{-\infty}^{+\infty} ae^{-\frac{(k_x - k_{xo})^2}{2\Delta}} \cos(k_x x + k_z z - \sigma_o t)\, dk_x \qquad (A.3.1)$$

where

a = amplitude factor

Δ = parameter controlling the width of the Gaussian packet. Delta is chosen to make the energy in the signal S fall to 10% of its peak value before the neighboring grid points in k space are reached. For $k_z(z) = k_{zo}$, the MLM produces a very sharp, and the conventional a reasonably sharp, peak in the power spectrum centered on k_{xo}, k_{zo}.

When

$$k_z(z) = (1 - \alpha \cdot z)\, k_{zo}$$

where α is chosen such-that k_z spreads over four grid points, MLM looses its sharp resolution. As seen in figure A.3.1, the depth dependency causes energy to spread not only into adjacent wavenumbers, but into those far removed from the original. Most of the peaks in figure A.3.1 have energy comparable to the original. The background level is raised from 40 decibels below the peak value to an average of only 5 decibels below. Due to

the heavy averaging properties of the conventional method, this linear variation in vertical wavenumber has a smaller effect on the resultant power spectrum. There are fewer spurious peaks and the background level is only minimally raised.

Both methods can be modified to include the same linear variation in vertical wavenumber which was in the input signal. In expression 5.2, the phase of the exponent $k \cdot x_i$ becomes

$$k_x \cdot x_i + k_y \cdot y_i + k_z \cdot (1 - \alpha z_i) \cdot z_i .$$

In both the estimator and in the artificial data, k_z varies in the same manner. Then the original, sharp packet is recovered.

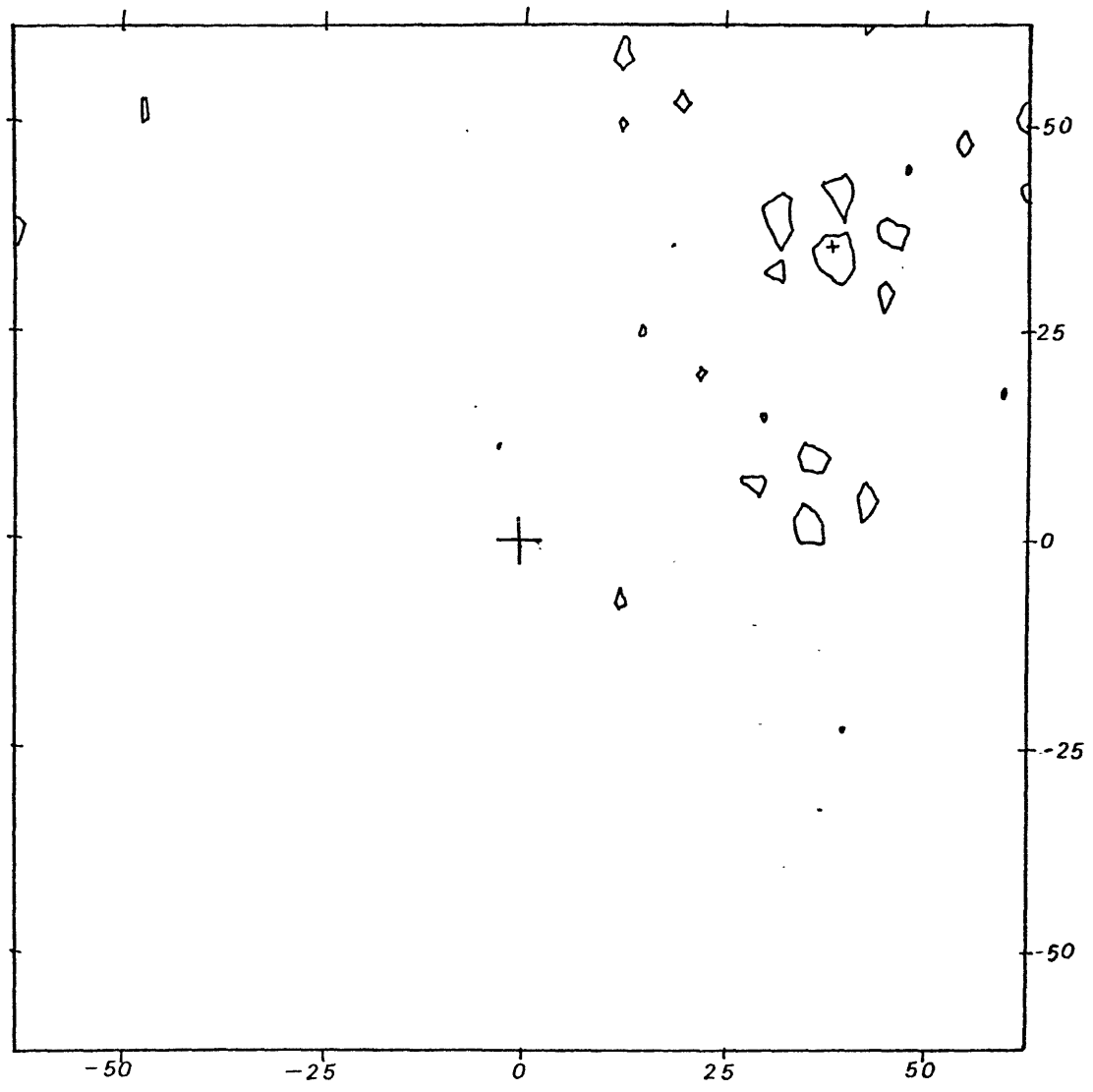

A.3.1 MLM realization of power spectra for a signal with a variable vertical wavenumber. The small + marks the position where the peak should lie.

APPENDIX A.4 Methods of and Confidence Limits for Modal Decomposition

Modal shapes are derived from a numerical calculation based on the Brunt-Väisälä profile (Jim Richman (personal communication)). The calculation uses rigid-lid, flat-bottom dynamics, and assumes there is no shear in the surrounding medium. With least squares, a set of modes is fit to currents and to isotherm displacements. For example, the east current, $E(z)e^{i\phi}$, is decomposed into real and imaginary components.

$$E(z)e^{i\phi} = E_R(z) + i\, E_I(z) \ .$$

The set of M equations

$$[E_R(z_i) - \sum_{j=1}^{N} A_j\, \psi_j(z_i)]^2$$

is minimized in a least squares sense.

$\psi_j(z_i)$ = normalized amplitude of mode j at depth i.

$E_R(z_i)$ = real component of current at depth i.

A_j = calculated weight of mode j in the decomposition.

N = number of modes to be fit.

M = number of instruments separated vertically.

Similar equations are used for the real and imaginary components of the north current (N), the Up isotherm (U), and the derived coherent isotherm displacement (PT), (Table 3.3). From the A_j's, the amplitude and phase of each mode, with respect to a particular start time, can be determined.

Theoretically, the amplitudes for up to M-1 modes may be calculated. Usually fewer modes can be stably fit. A stable fit occurs if, when the number of modes (N) is varied, the amplitude and phase of those remaining do not radically alter. The percentage residuals

$$G(z_i) = 1 - \frac{\sum_{j=1}^{N} A_j \, \psi_j(z_i)}{E_R(z_i)}$$

should be small. Nor should the ratio of the sum of the magnitudes of the modal currents to the measured current

$$H_i = \frac{\sum_{j=1}^{N} |A_j \, \psi(z_i)|}{|E_R(z_i)|}$$

be far from unity. If H, on average, is much greater than one, the decomposition implies there is much more energy in the field than actually measured.

The above confidence tests indicate whether a specific decomposition is valid. They also serve to determine which decomposition in a set is the best. The significance levels are determined by decomposing several sets of random numbers,

Gaussionaly distributed about zero with a variance equal to the IWEX record variance, into normal modes.

All of our decompositions tested better than the random numbers, though U<3> is marginal. The low modal content of our signals argues against their being noise, for high modes dominate the random number fit. Table A.4.1 lists the relevant confidence tests for PT, U<3>, and the random numbers. Because the spread in magnitudes of the signals was much larger than for the random numbers, all $H(z_i)$'s greater than 2 or less than 1/2, and all $G(z_i)$'s larger than one were considered equally bad.

Data from instruments on leg A were formed into signals similar to the U's, which are averaged across the mooring. In all cases, the modal decomposition was similar, but the confidence tests were worse than those of the U's.

TABLE A.4.1

Modal Confidence Levels

Signal Conf. Test	Level 4	Level 5	Level 6	Level 10	Level 12	Level 14	Level 15
PT_R							
$H(z_i)$	2.6		1.1	1.2	.98	.99	1.4
$G(z_i)$	.57		.26	.06	.02	.01	.03
PT_I							
$H(z_i)$	1.4		1.1	1.6	80.	2.9	1.7
$G(z_i)$	.08		.11	.12	1.8	0	.01
$U<3>_R$							
$H(z_i)$	2.8	2.2	.97	.94	1.1	1.1	1.1
$G(z_i)$	.62	.39	.28	.06	0	.04	.08
$U<3>_I$							
$H(z_i)$	1.1	.93	.93	1.6	17.8	21.	2.3
$G(z_i)$	.07	.07	.11	.04	3.4	3.0	.04
RN_1							
$H(z_i)$	.79	1.6	.4	2.4	3.2	2.	1.6
$G(z_i)$	.22	2.6	.6	.1	.66	.01	.17
RN_2							
$H(z_i)$	.41	6.2	.85	.69	1.7	.96	4.3
$G(z_i)$	.96	.53	.47	.91	.71	.18	.01

APPENDIX A.5 Mode Fitting to an Asymmetric Energy Field

A simple model may serve to illustrate how modes can be fit to a field with an asymmetric energy distribution in k_z. Let the field be composed of two waves,

$$\xi = \cos(k_{x_o} x + k_{z_o} z - \sigma_o t) + A \cos(k_{x_o} x - k_{z_o} z - \sigma_o t)$$

In the above, the first wave carries energy toward the ocean floor and the second carries it toward the surface. The above may be reformulated

$$\xi = (A+1)\cos(k_{x_o} x - \sigma_o t)\cos(k_{z_o} z) + (A-1)\sin(k_{x_o} x - \sigma_o t)\sin(k_{z_o} z)$$

$$= (A+1)\cos(k_{z_o} z) - i(A-1)\sin(k_{z_o} z)\, e^{i(k_{x_o} x - \sigma_o t)}$$

where

$$\cos(k_{z_o} z_{top}) = \cos(k_{z_o} z_{bottom}) = 0 .$$

When A = 1, we recover a simple, modal depth variation.

If $A \neq 1$ we can still fit the above field with a sum of orthonormal modes. If A is approximately one, this fit would be

dominated by the proper mode, i.e., the mode with depth variation equal to $\cos(k_{z_o} z)$.